A Sparse Synthetic Aperture Radiometer Constellation Concept for Remote Sensing of Antarctic Ice Sheet Temperature

Alex B. Akins, *Member, IEEE*, Alan B. Tanner, Andreas Colliander, *Member, IEEE*, Nicole-Jeanne Schlegel, Kenza Boudad, Igor Yanovsky, Shannon T. Brown, *Senior Member, IEEE*, and Sidharth Misra, *Senior Member, IEEE*

***Abstract*— We present a concept for UHF/L-band (0.5–2 GHz) remote sensing of Antarctic ice sheet internal temperature using a highly sparse synthetic aperture radiometer constellation. This concept leverages the relative stability of ice sheet thermal emission over long temporal periods to gradually assemble a collection of array baselines which are jointly transformed to develop large image facets. We formulate a calculation of minimum array complexity based on the desired sensitivity, spatial resolution, and time available for observations. We determine from this calculation that such a system can achieve 1–10-km spatial resolution (significantly finer than the program of record) over monthly to yearly timescales with as few as 10–20 elements; even fewer elements are required for observing only the ice sheet center. The inverse problem of reconstructing image facets from mixed-pointing and mixed-configuration observations is posed using a Fourier domain data constraint with a total variational regularization in the image domain. This approach enables image formation from heterogeneous observations while mitigating artifacts. We present a notional constellation design for three satellites which could accomplish the necessary baseline sampling by rotating the phase and semimajor axis of spacecraft relative positions in planar circular orbits (PCOs). We demonstrate image formation by observing system simulations leveraging predictions of Antarctica's multiwavelength brightness temperature computed from ice sheet thermomechanical and radiative transfer models.**

***Index Terms*— Antarctica, constellation, interferometry, microwave radiometry, sparse.**

I. Introduction

THE Antarctic ice sheet plays a crucial role in the long-term storage of water and in the energy balance of the Earth system [1]. For this reason, environmental monitoring and space agencies around the world have prioritized observation of ice sheet properties and accurate prediction of their change over time. Contemporary observational studies of ice sheet dynamics leverage gravimetry, altimetry, and synthetic aperture radar data to infer ice sheet mass, surface elevation, thickness, and velocity [2], [3], [4], [5], [6]; these measurements observationally constrain overall mass balance. Ice sheet internal temperatures, however, had not been inferred over large spatial extents prior to the analysis of [7], who used soil moisture and ocean salinity mission (SMOS) single-wavelength L-band radiometry as a proof of concept. Further spacecraft remote sensing observations of ice sheet temperatures with a dedicated instrument would be of great use, as high-precision borehole measurements of deep ice temperatures are sparse, and large differences exist in sheet base geothermal heat fluxes (GHFs) inferred from in situ, gravimetric, seismometric, and magnetometric observations [8], [9], [10]. Such observations could help determining the contributions of ice deformation and basal slip to total ice velocity and identify critical regions of thaw near the sheet bed [11]. These improved estimates of the ice sheet's thermal and basal conditions would increase confidence in model projections of future dynamic ice response to changes in climate [11], [12], including large-scale ice sheet retreat due to warming and contribution to global mean sea level.

Water ice has a low dielectric loss, making it highly transparent to microwave radiation [13]. Recognizing this, the microwave remote sensing community has explored the prospects of ice sheet internal temperature remote sensing using multiwavelength microwave radiometry [14]. Recent 0.5–2-GHz (UHF/L band) microwave radiometer aircraft experiments over Greenland have demonstrated temperature sounding capabilities from the surface to near the base of the sheet [15], [16], resulting in a marked improvement over the single-wavelength observations of [7]. The success of these experiments has driven interest in a space mission centered around this measurement [17]. However, radiometers are diffraction-limited systems, and for UHF/L-band observations from space, observations with 1–10-m scale antennas translate to surface spatial resolutions of a few to several tens of kilometers. While observations at these resolutions can characterize broad spatial variations in ice sheet thermal emission, they would not resolve heterogeneity on fine scales, including, e.g.,

Received 20 September 2024; revised 18 December 2024 and 14 January 2025; accepted 23 January 2025. Date of publication 28 January 2025; date of current version 10 February 2025. This work was supported in part by the NASA Instrument Incubator Program Award to JPL titled "Separated Thinned Array for Sensing of Ice Sheets (STASIS)" under Grant 87-110967; and in part by the Jet Propulsion Laboratory, California Institute of Technology, through a contract with the National Aeronautics and Space Administration under Grant 80NM0018D0004. *(Corresponding author: Alex B. Akins.)*

Alex B. Akins, Alan B. Tanner, Andreas Colliander, Kenza Boudad, Igor Yanovsky, Shannon T. Brown, and Sidharth Misra are with the Jet Propulsion Laboratory, California Institute of Technology, Pasadena, CA 91109 USA (e-mail: alexander.akins@jpl.nasa.gov).

Nicole-Jeanne Schlegel is with the NOAA Geophysics and Fluid Dynamics Laboratory, Princeton, NJ 08540 USA.

Digital Object Identifier 10.1109/TGRS.2025.3534466

topographically induced variability and compact hotspots in glacier bed GHF [18], [19], [20].

Synthetic aperture radiometer systems become a practical alternative to scanned real aperture designs when aiming for finer spatial resolution. While synthetic aperture arrays are generally sparse in astronomy applications, the sensitivity required to observe atmospheric and hydrological variables on Earth (which are highly temporally variable) necessitates arrays that provide full spatial frequency coverage (within a finite support) [21], [22]. This requirement motivated the design of the microwave imaging radiometer with aperture synthesis (MIRAS) instrument for the SMOS mission [23], [24] and several demonstrator/aircraft instruments, such as ESTAR [25], 2D-STAR [26], HUT-2D [27], PAU-SA [28], GeoSTAR [29], IMR [30], and others (excluding for brevity several variable baseline demonstrators, see [31]). Unconventional approaches have also been conceived to improve the observation spatial frequency coverage, such as formation flying for high-resolution systems [32], [33], rotationally scanned arrays [34], [35], multidelay correlations [36], [37], or some combination of these [38], [39].

Unlike other components of the global water cycle, ice sheets are relatively stable over long periods of time. Spatiotemporal variability occurs in near-surface melt cycles [40], but these do not extend into the inner ice sheet, where ice temperature profiles record histories of climate change [41], [42]. The relative temporal and spatial stability of ice sheet temperatures, combined with the rapid revisit time of polar-orbiting spacecraft over Antarctica, might relax the snapshot spatial frequency coverage and sensitivity requirements incumbent on Earth-sensing interferometers. It is therefore conceivable that a sparse array could recover images over Antarctica at high resolution by iterating through several configurations, much like the earliest radio interferometer systems for astronomy.

In this article, we consider such a concept for UHF/L-band synthetic aperture radiometry remote sensing of ice sheet temperatures with a sparse satellite constellation. This concept consists of multiple satellites equipped with wideband antenna elements operating from 0.5 to 2 GHz (with spectral characteristics similar to instrument discussed in [43]) flying in the close formation in highly inclined orbits. Measurements from each antenna are transmitted to a correlator, housed within one of these spacecraft, to form interferometric baselines. Between overpasses of Antarctica, the constellation spacecraft cycle through multiple configurations, filling out a broad range of measured spatial frequencies over time. Our results suggest that, with sufficient maturation to the key enabling technologies, such an array could be designed to obtain spatial resolutions as fine as 1 km over seasonal-to-yearly timescales. Such fine resolution would provide a significant improvement over the program of record for L-band radiometry and open new research avenues in glaciology. Our discussion is structured as follows.

1) Section II discusses the characteristics, with an emphasis on temporal stability, of 0.5–2-GHz ice sheet band brightness temperatures based on prior observations and ice sheet thermomechanical and radiative transfer simulations.
2) Section III discusses relationships among synthetic aperture radiometer array complexity, observation duration, and achievable sensitivity and spatial resolution for resulting images.
3) Section IV addresses the problem of stitching many satellite overpasses—each of the partial Fourier coverage and of partial overlap—together. We present a hybrid Fourier-domain data constraint and image-domain regularization formulation of the image reconstruction problem which can accommodate this heterogeneous approach.
4) In Section V, we present a notional formation-flying constellation design for sampling a range of array spatial frequencies and assess this design with orbital simulations.
5) Section VI, we present observing system simulations investigating different aspects of the concept to demonstrate the proposed approach.

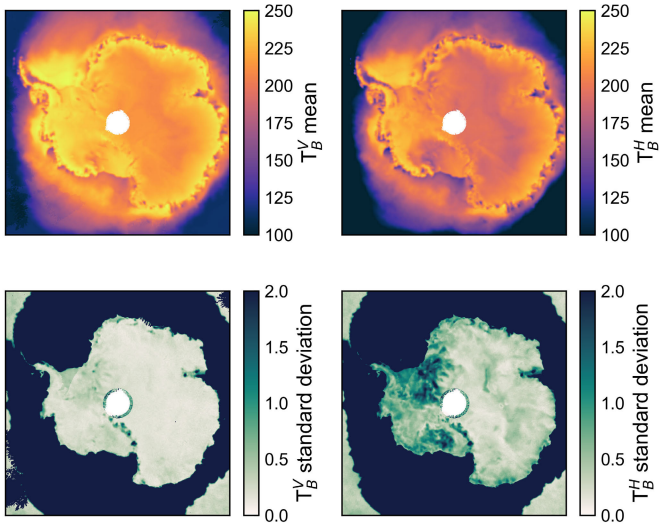

Fig. 1. Annual mean and standard deviation of SMAP dual-polarized 40° brightness temperatures, indicating seasonal stability over much of the sheet.

II. Antarctic Ice Sheet Characteristics

The 0.5–2-GHz brightness temperatures (T_B's) of an ice sheet are dependent on its temperature profile [44], and since the internal temperatures of multiyear ice structures vary little, we would expect the same to be true of the UHF/L-band T_B's. This is confirmed observationally, with a SMOS validation campaign at Dome-C finding annual standard deviations of 0.45 and 1.5 K for in situ tower measurements of V- and H-pol T_B at 42° incidence angle [45]. We show in Fig. 1 the 2021 annual mean and standard deviations of Antarctic L-band T_B's as observed by SMAP (averaged over monthly timescales to isolate the seasonal variations from instrument noise), illustrating that similar stability is observed in the space mission program of record. For shallower observing incidence angles, we expect annual deviations in ice sheet brightness temperatures to be of order 1 K, falling between the values observed by Macelloni et al. [45]. For steeper incidence angles, however, horizontally polarized observations may exhibit regional fluctuations that are much larger than 1 K [46]. Exceptions

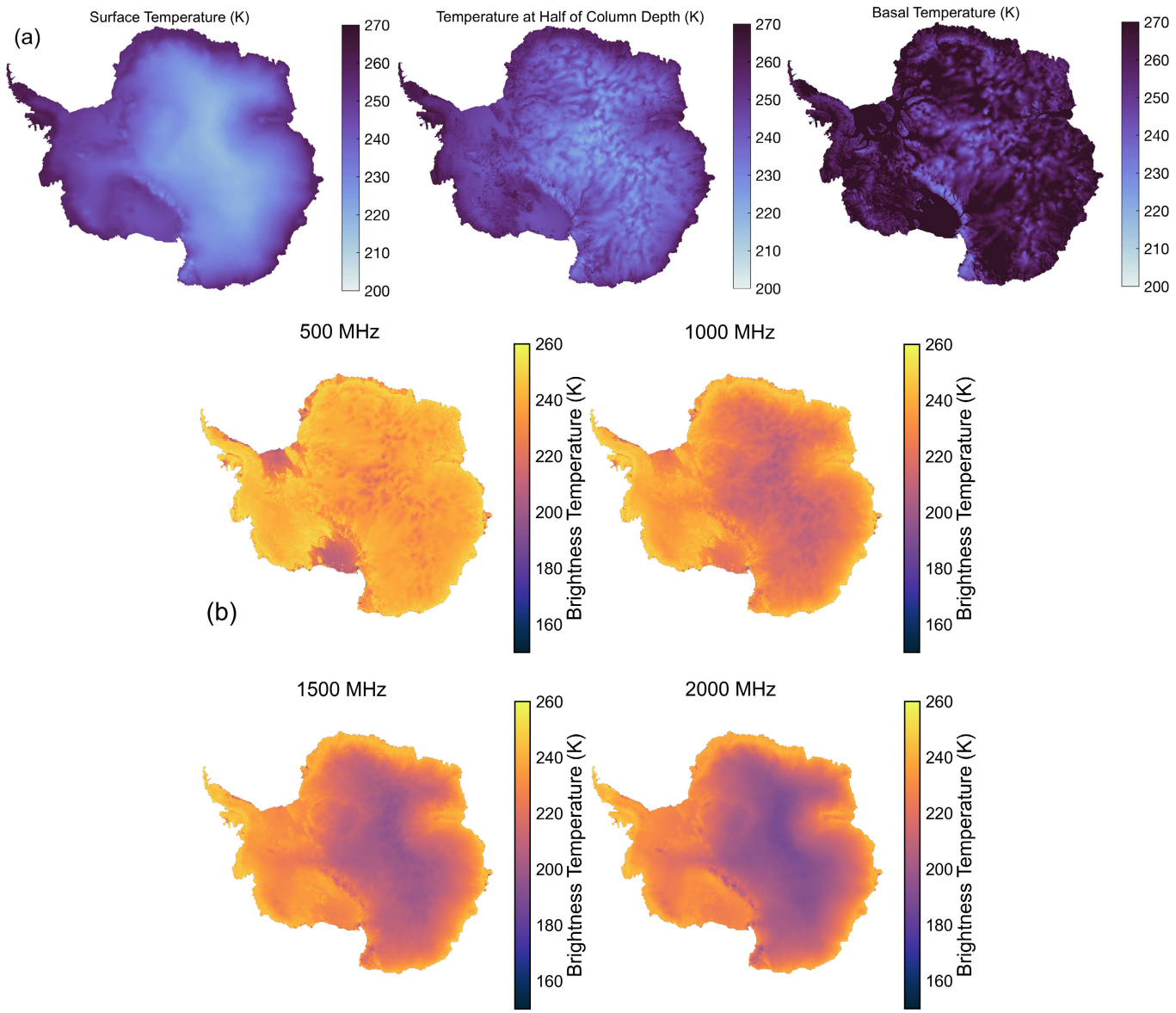

Fig. 2. (a) Surface, middle-layer (half of the ice column depth), and basal ice sheet temperatures at southern solstice computed using the GEMB-ISSM model. (b) Multiwavelength nadir brightness temperature images of the Antarctic ice sheet computed using the MEMLS model.

to the stability of L-band Antarctic T_B's, as evidenced in comparison of the top and bottom rows of Fig. 1, result from seasonal melt. However, significant melting only affects the outer 5% of the Antarctic ice sheet surface area and regional melt events occur on the order of 20 days per year [47]. This implies that melting will not obscure observations of many near-shelf ice features of interest with unknown extents of bed thaw [11].

To further assess the characteristics of ice sheet UHF/L-band thermal emission, we computed a high-resolution model of Antarctica's T_B from 0.5 to 2 GHz. Ice temperature and density profiles were determined using the ice-sheet and sea-level system model (ISSM), a thermomechanical finite-element model that simulates continental ice temperature and flow [48]. The continental simulation mesh resolution is 1 km or finer at the domain boundary and within the shear margins, with a maximum resolution of 50 km in the interior. For the simulation of the thermal and mass evolution of the snow and firn layer of the Antarctic ice sheet, we use ISSM's glacier energy and mass balance (GEMB) module [49]. The GHF map from [50] is used as a lower boundary. Fig. 2(a) shows the cross sections of the derived 3-D ice sheet temperatures for the top, middle (50% of the ice thickness at each grid point), and bottom layers of the southern hemisphere solstice simulations. We note that since each spatial pixel has a separate vertical grid, the middle layer temperature in Fig. 2(a) does not correspond to a fixed depth.

These model profiles were used as inputs to the microwave emission model for layered snowpacks (MEMLSs, see [51]) radiative transfer model to compute polarized T_B's. The MEMLS model uses a variety of physical and empirical models to translate inputs of temperature, density, and exponential correlation length of the ice microstructure into scattering, absorption, and reflection coefficients for each layer. These

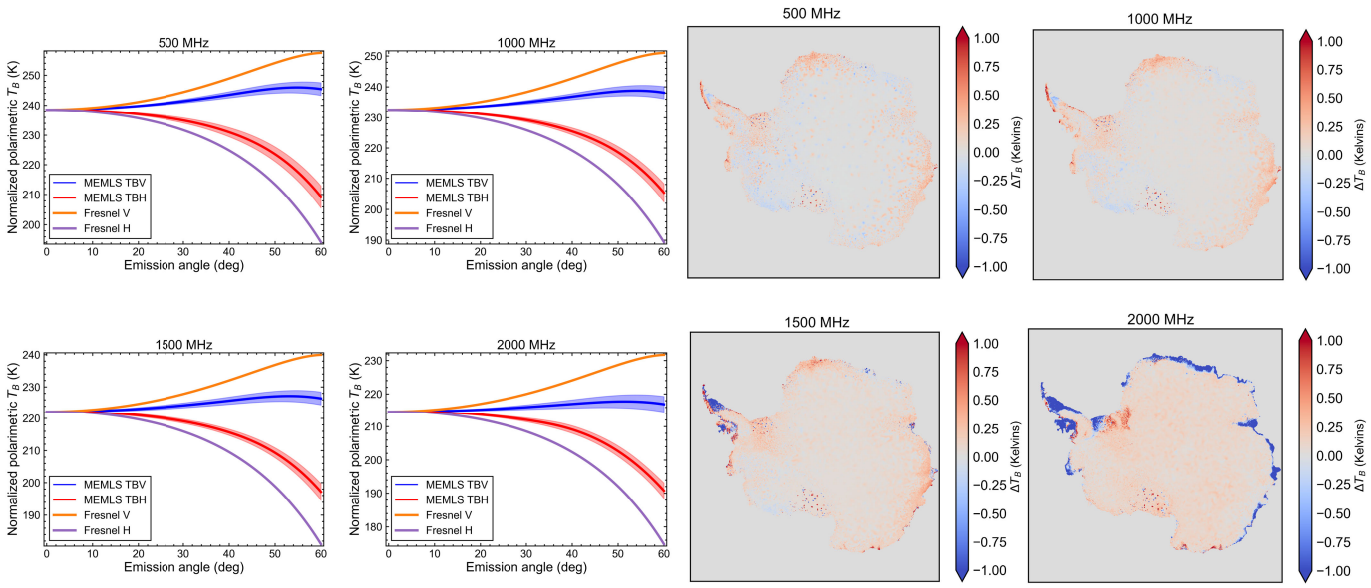

Fig. 3. (Left) Mean and standard deviation of modeled ice sheet polarimetric brightness temperatures versus emission angle as compared with Fresnel reflection for a specular dielectric interface. (Right) Differences per 1-km pixel in modeled nadir ice sheet brightness temperature between Antarctic summer and winter.

properties are then used to compute the layer-integrated T_B. To improve the accuracy of the multiwavelength T_B simulations, the MEMLS simulations were tuned to match SMAP observations at 1.4 GHz and 40° incidence angle. This tuning was based on adjusting the exponential correlation length of the snow microstructure (positively correlated with layer internal scattering) in the simulation inputs. An average firn correlation length near 0.3 mm was found to best reproduce the L-band brightness temperatures observed by SMAP. Since we are only interested here in an approximate estimation of ice sheet thermal emission, detailed tuning of MEMLS parameters for different spatial regions was not undertaken. Resulting brightness temperature maps are shown in Fig. 2(b) and are qualitatively consistent with those of [52].

Full sheet T_B's were also simulated at emission angles between 0° and 60° to estimate tolerances for the maximum overlapping difference in surface incidence angles in combining heterogeneous observations (discussed further in Section IV). From the results in Fig. 3, we determine that differences in the field of view incidence angles of more than 15° in the case of single polarization measurements and 30° in the case of dual-polarization measurements might introduce biases of greater than 1 K in the recovered image. As we discuss later, however, this effect can be somewhat mitigated through the use of an approximate incidence angle-dependent compensation. Fig. 3 also shows the results of an additional test whereby the difference in simulated nadir T_B's between the Antarctic summer (July 2021) and winter (January 2022) were taken. These results are consistent with previously discussed observational constraints in suggesting that seasonal changes in L-band ice sheet T_B's are expected to be low if observed at relatively shallow incidence angles. This affirms the core assumption of our measurement concept.

III. Bounding Limits on Sensitivity Versus Spatial Resolution

With the intuition developed in Section II for Antarctica's thermal emission characteristics, we can now address considerations for array design. We introduce the standard definitions for synthetic aperture radiometry, providing also a few visual definitions in Fig. 4.

Synthetic aperture radiometers measure the complex correlation of electromagnetic radiation (with frequency f and wavelength λ) received by antennas at separate locations. These correlations represent discrete components of the Fourier series corresponding to the angular distribution of the received radiation. By employing an array to measure pairwise correlations between several different baselines, the Fourier representation is improved, and the true angular distribution of received radiation can be recovered. Corbella et al. [53] provide an expression for the complex correlation function $\langle E_i E_j^* \rangle$ (or the "visibility" function $V_{i,j}(u, v)$, interchangeably) which is the fundamental measurement of an interferometer system. For uncoupled receiving elements and a scene in the far field, this expression as follows:

$$\begin{aligned} \langle E_i E_j^* \rangle &= V_{ij}(u, v) \\ &= \iint \frac{T_B'(l, m)}{\sqrt{1 - l^2 - m^2}} r_{ij}(ul + vm) e^{-j2\pi(ul+vm)} \mathrm{d}l \mathrm{d}m \\ T_B'(l, m) &= \frac{T_B(l, m) F_i(l, m) F_j^*(l, m)}{\sqrt{\Omega_i, \Omega_j}}. \end{aligned} \tag{1}$$

Here, $T_B(l, m)$ is the spatial distribution of the scene T_B with angular coordinates l and m, which are the direction cosines with respect to the axes of the array plane. The array elements are located to measure baselines with spatial frequencies u and v, which are defined in wavelengths. $F(l, m)$ represents the field pattern for the receiving antennas and Ω is the integral of the square of the field patterns over a solid

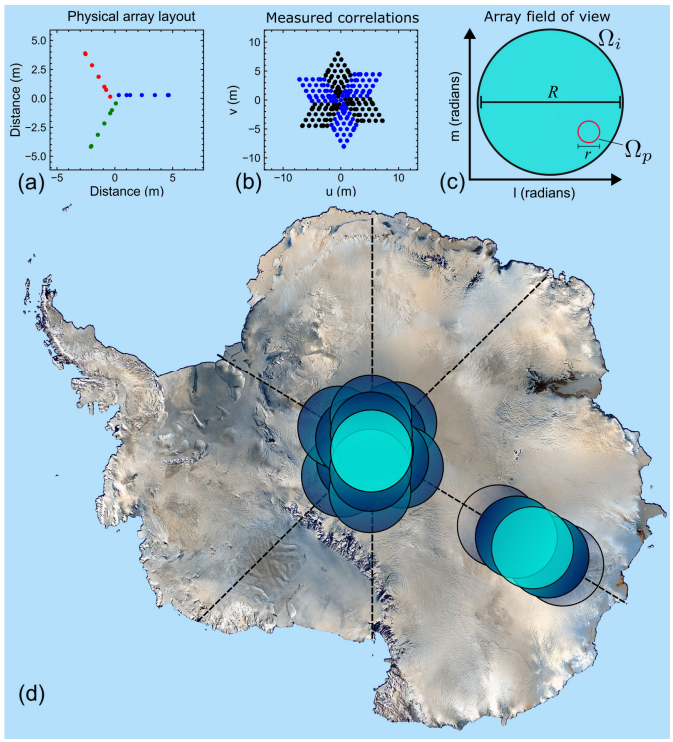

Fig. 4. Illustration of geometries relevant to the observation concept. Each satellite in the constellation will include a subarray with some arbitrary element geometry [e.g. (a)]. Correlation of measurements both within (b) and between (not shown) subarrays yields samples of the image Fourier harmonics with spatial frequencies u and v. The field of view of the array (c) has solid angle Ω_i, swath width R and is composed of pixels with solid angle Ω_p and spatial resolution r. The field-of-view coordinates are the direction cosines l and m relative to the array pointing center. (d) Large image facets are constructed by combining measurements from different swaths. Depending on the orbital geometry and the swath size, the constellation revisit near the antarctic pole is greater than at the edge of the sheet. (Antarctica image: NASA Earth Observatory.)

angle. Finally, $\widetilde{r}_{ij}$ is a baseline-dependent smearing function, also referred to as the "fringe-washing" function, resulting from averaging measurements over some bandwidth (i.e., not monochromatic) or time. For a finite number of measured correlations, neglecting fringe wash, the corresponding brightness temperature distribution can be recovered via the direct sum of the Fourier series

$$T_B'(l,m) = \sum_{k}^{n_v} V(u_k, v_k) e^{j2\pi(u_k l + v_k m)} \tag{2}$$

where n_v is the number of spatial frequency samples. We note that n_v is twice the number of measured correlations as a result of conjugate symmetry in the Fourier transform of real signals. Since noise in both the real and imaginary parts of the complex correlation is independent, however, the number of degrees of freedom in the measurement remains n_v.

With these definitions, we now consider the implications of the synthetic aperture sensitivity equation for the proposed concept. Readers interested in a thorough derivation of this equation should refer to the expositions of [21], [22], and [54]. Assuming the usual idealizations (e.g., equal weighting of all correlations and neglecting several system efficiency terms), the sensitivity of a brightness temperature image is as follows:

$$\Delta T_B = \sqrt{n_p} \frac{T_B + T_R}{\sqrt{B\tau}} \tag{3}$$

where n_p is the number of independent image pixels, T_B is the scene mean brightness temperature, T_R is the receiver noise temperature, B is the receiver bandwidth, and τ is the system integration time. In the case of a zero-redundancy imager, where all measured correlations represent unique spatial frequency samples, [21], $n_p = n_v$, which is the formulation commonly encountered in the Earth remote sensing literature. This equation is valid for both real, synthetic, and mixed (e.g., scanned beamformer) aperture observations due to their fundamental equivalence [55]; both real and synthetic aperture systems need to observe the same number of total pixels for the same amount of total time to achieve equal sensitivity. Departures from the zero-redundancy formulation can be incorporated by including a spatial frequency sampling efficiency term $E_V = n_v/n_p$ under the root in the denominator of (3). It is assumed that any gains or losses in E_V are spread equally across the range of measured spatial frequencies (i.e., an increased number of measurements of one visibility sample would not significantly improve image sensitivity). Incorporating this term and simplifying it with the definition of n_p as the ratio between the image area Ω_i and the pixel area Ω_p gives

$$\Delta T_B = \frac{\Omega_i}{\Omega_p} \frac{T_B + T_R}{\sqrt{n_v B\tau}}. \tag{4}$$

For application to our concept, we can establish nominal values of some of the terms in (4) from the results of prior UHF/L-band ice sheet radiometry aircraft experiments [16], [43]. For these experiments, retrievals were conducted from observations with $B = 100$ MHz wide spectral channels and total system temperatures on the order of $T_B + T_R = 1000$ K, achieving $\Delta T_B = 1$ K.

We are primarily interested in the relationship between spatial resolution via Ω_p and orbital altitude, the instantaneous field of view via Ω_i, the number of necessary array elements, and total observing time. We note that Ω_i is the lesser of either the elemental antenna solid angle or the angular extent of the observable Earth. To convert between per-correlation integration τ and real total observation time t, we introduce an orbital efficiency factor E_{orb} such that $\tau = E_{\text{orb}} t$ in (4). E_{orb} is defined as the fraction of time during spacecraft operation where the spacecraft can observe emission from within a particular field of view over the Antarctic continent. In the limiting case for which the whole Antarctic continent can be observed simultaneously, E_{orb} is determined by the period for which the southernmost latitudes are in view of a polar orbiting spacecraft ($E_{\text{orb}} \approx 0.1$). For observations in low Earth orbit, where the entire continent is not viewed at once, we determine E_{orb} using a numerical orbital simulation. A 90° inclined orbit is assumed, and the array field-of-view equivalent surface area is assumed to be the geodesic circle containing all surface pixels within a prescribed range of observation incidence angles. If a pixel falls within the field of view mask, a count is added, and the final count represents the

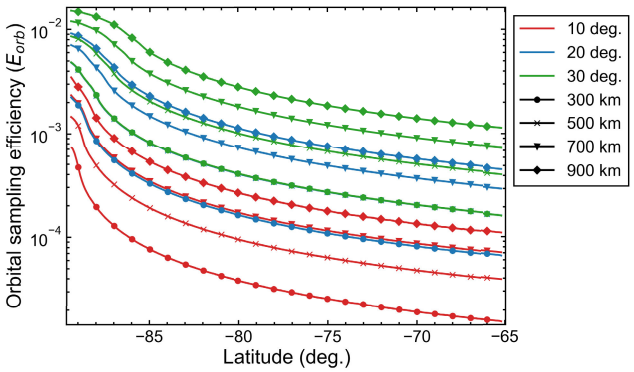

Fig. 5. Computed orbital sampling efficiency factor E_{orb} as a function of latitude for different spacecraft orbital altitudes and maximum swath surface incidence angles.

total number of seconds that the pixel was "observed." Since we are interested in the amount of time spent over the field of view, each pixel count is weighted as the fractional area between a swath centered at the pixel and a swath centered at the field-of-view center using the equation for the area of two overlapping circles. This area ratio changes with the swath size, but in the limit of a large swath, it is unity, so the use of the smaller swath overlap is conservative. Fig. 5 shows the computed ratio E_{orb} of total time counted over a swath area divided by the total simulation time for different orbital altitudes as a function of latitude.

We use these values for E_{orb} at the edge and the center of the sheet to determine how much time is needed to obtain $\Delta T_B = 1$ K with a given number of antennas. Expressions for the minimum observing time t and number of antennas N needed [assuming $n_v = N(N-1)$] can be obtained by rearranging (4) as follows:

$$t_{\text{sens}} \geq \frac{R^4}{r^4}\left(\frac{T_B + T_R}{\Delta T_B}\right)^2 \frac{1}{B E_{\text{orb}} N(N-1)} \tag{5}$$

where R is the swath width and r is the spatial resolution. We can similarly compute the time necessary to obtain full spatial frequency sampling assuming array reconfiguration once every t_r seconds and that each array reconfiguration samples a unique set of baselines as follows:

$$t_{\text{samp}} \geq \frac{R^2}{r^2}\frac{t_r}{N(N-1)}. \tag{6}$$

Results of these calculations are summarized in Fig. 6 for observations at 500 MHz. While our concept entails measurements from 0.5 to 2 GHz, we consider here solely the lower end of this range since it represents the limiting case, as an arbitrarily sized array will obtain its coarsest spatial resolution at the lowest frequency. Fig. 6 can be quickly used to identify feasible ranges for observing time, array size, and antenna diameter corresponding to the desired spatial resolution. Some important overarching results from Fig. 6 include the following.

1) Lower altitude LEO orbits are preferred for observing system design. The decrease in pixel solid angle for higher orbital altitudes imposes limits on sensitivity that are not balanced by the relative increase in orbital coverage. In the limiting case of a medium earth orbit (MEO) with $E_{\text{orb}} = 0.1$ [Fig. 6(c)], achievement of a 10-km spatial resolution requires a large array system.
2) Large apertures can attain a given sensitivity with fewer receiving elements in a given time span, but only on average and in trade for a narrower field of view that may reduce orbit coverage.
3) As expected from Fig. 5 and the illustration in Fig. 4, significantly less observing time is necessary to obtain sensitive observations at the center of the ice sheet due to the higher orbital sampling efficiency at the center.

From (5), the amount of additional time (for an array using the same number of elements and targeting the same per-pixel sensitivity) to improve the spatial resolution of an observation by an order of magnitude is 10^4 s, whereas from (6), the extra time necessary to achieve the corresponding Fourier coverage for this higher spatial resolution is of order 10^2 s. The square root of these ratios applies when discussing this trade in terms of increasing the number of array elements.

From Fig. 6(a) and (c), we identify a few interesting schemes of array operation.

1) A small aperture (half-wavelength) system consisting of 10–20 antennas that achieves 10-km resolution over the full ice sheet on seasonal-yearly timescales. The maximum baseline separation would range between 20 and 30 m.
2) A medium aperture system (one wavelength) system consisting of 15–25 antennas which achieve 5-km resolution over the full ice sheet on monthly seasonal timescales. The maximum baseline separation would range between 40 and 60 m.
3) A large aperture system (two wavelengths) consisting of 20–30 antennas which achieve 2-km resolution over the full ice sheet on monthly seasonal timescales. The maximum baseline separation would range between 100 and 150 m.
4) A small/medium aperture system consisting of 3–5 antennas which achieves <10 km resolution over the sheet center on seasonal/yearly time scales.

For each scheme above, the maximum baseline separations are determined so as to achieve the stated spatial resolution in the 500-MHz channel. Sub-kilometer spatial resolutions at 1-K sensitivity would not be achievable over annual timescales for all but the largest array element numbers and aperture diameters (ADs), corresponding to upper bounds on constellation separation distances on the order of 500 m in low Earth orbit. This eliminates array geometries based on constellations in distinct orbits, especially considering the significant reduction in observing time imposed by such a configuration. We also note that correlations measured between array elements on spacecraft traveling past each other at kilometers/second speeds would incur significant decorrelation/fringe wash for integrations longer than a few tens of microseconds.

To conclude, our first-order assessments of necessary array tolerances and achievable sensitivities suggest that a separated constellation array should be capable of obtaining 1–10-km surface spatial resolution within one year of observation time.

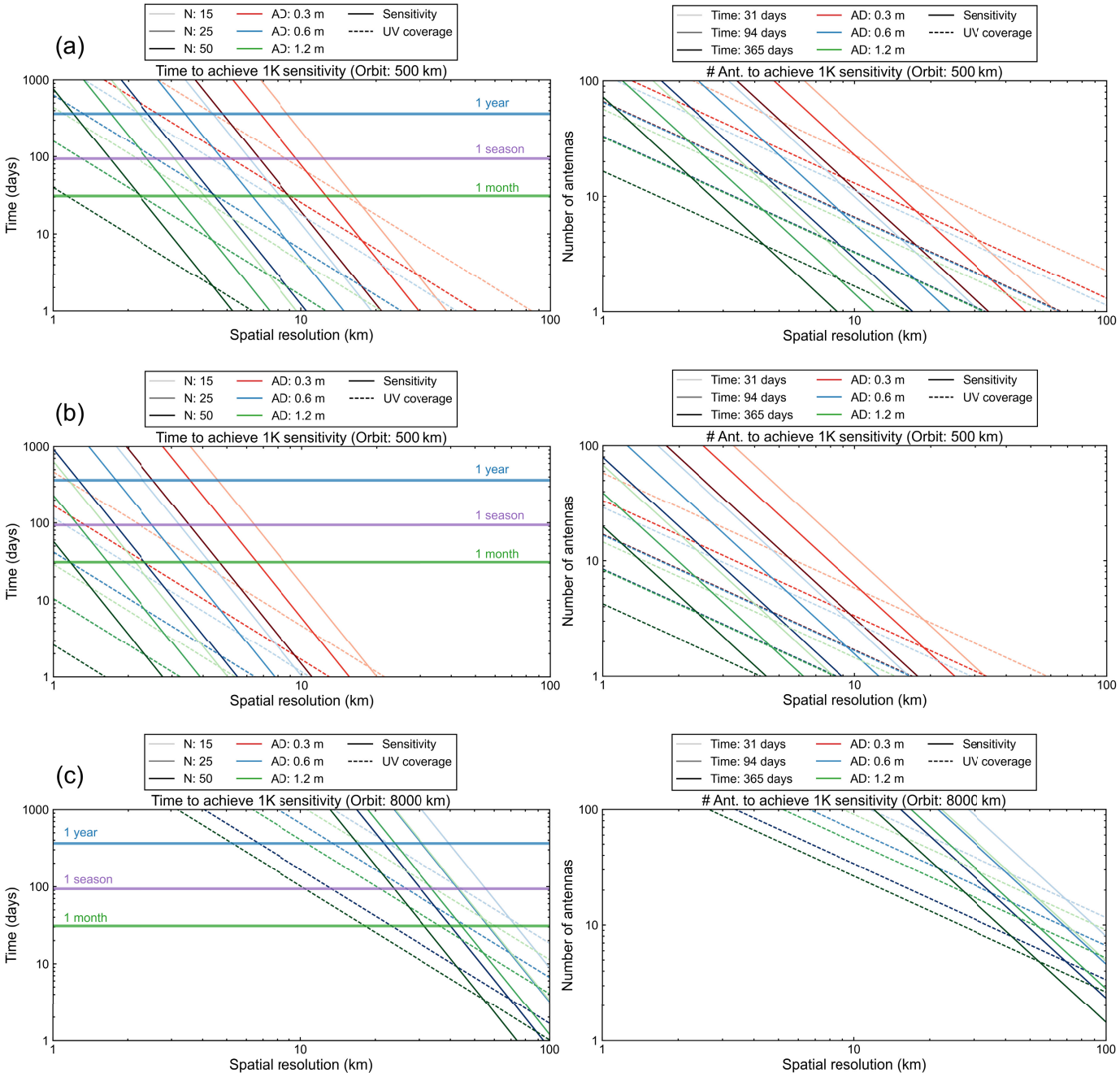

Fig. 6. Relationships, computed using (5) and the orbital efficiencies in Fig. 5, between observing time in real days (left column) and a number of array elements (right column) necessary to obtain $\Delta T_B = 1$ K for $f = 500$ MHz at a given spatial resolution for (a) full ice sheet at an orbit altitude of 500 km, (b) center of the ice sheet at an orbit altitude of 500 km, and (c) full ice sheet at an orbital altitude of 8000 km. The solid lines represent the sensitivity calculations from (5), and the dashed lines represent the time/sampling to achieve full spatial frequency coverage assuming reconfigurations each day (each orbit for the center of the sheet) from (6). Curves of different color correspond to different array element ADs. Note in (c) the equivalence of the 0.3- and 0.6-m AD lines, as the half-power fields of view for both of these aperture sizes exceed the horizon.

Observations in low orbits with larger apertures are favored. While observations targeting the entire ice sheet will require no fewer than ten elements, observations targeting the center of the ice sheet, where revisits are at their highest, should be capable of obtaining spatial resolutions within 10 km with as few as 3–5 elements.

IV. Combining Heterogeneous Observations

An important consideration for this concept is the method for forming images from disaggregated array measurements. As reviewed in Section III, T_B images can be formed from interferometric observations via Fourier transform of the measured correlations as in (2), assuming a forward model of (1) in which all image harmonics are contained within a single, common elemental antenna footprint. The problem posed by our concept is that different spatial harmonics are now measured within different footprints. These measurements must somehow be "stitched" together into a final image.

We begin by restating the forward model of the measurements (1) in terms of an array transfer function matrix $\mathbf{G}$. The

matrix $\mathbf{G} \in \mathbb{C}^{n_v \times n_p}$ is a Riemann sum approximation to the continuous integral response of the interferometer array [56] which relates the image $\mathbf{T} \in \mathbb{R}^{n_p \times 1}$ to the measured correlations $\mathbf{V} \in \mathbb{C}^{n_v \times 1}$.

$$\mathbf{V} = \mathbf{GT}. \tag{7}$$

For fully or over-sampled conventional arrays, an image can generated from measurements $\mathbf{V}$ via a conditioned inversion of the $\mathbf{G}$ matrix [57]. Application of this approach to our concept might involve the inverse transform of an under-sampled $\mathbf{G}$ matrix (via the projection theorem) for each footprint and averaging these results in the image domain. This is similar to the well-developed "mosaicking" problem in radio astronomy, wherein images determined from multiple pointings with an array are averaged as weighted by the array antenna patterns [58], [59]. However, this mosaic approach is contingent on averaging images with similar point spread functions, which is violated here.

Instead, we consider a formulation of (7) which relates all measured visibilities to the scene image using a composite structure for the $\mathbf{G}$ matrix. For each integration period of the array, a separate $\mathbf{G}_k$ matrix is established. The matrix $\mathbf{G}$ is then a rowwise stack of individual $\mathbf{G}_k$, expressed as follows for an array with uncoupled, identical antenna elements with normalized pattern $\bar{F}^2(l, m) = F^2(l, m)/\Omega$

$$\mathbf{G} = \begin{bmatrix} \mathbf{G}_1 \\ \cdots \\ \mathbf{G}_N \end{bmatrix} = \begin{bmatrix} A_{ij1} e^{-j2\pi\left(u_{1,i} R_{1,1} l_j + v_{1,i} R_{1,2} m_j\right)} \\ \cdots \\ A_{ijN} e^{-j2\pi\left(u_{N,i} R_{N,1} l_j + v_{N,i} R_{N,2} m_j\right)} \end{bmatrix}$$
$$A_{ijk} = M_{k,j} \bar{F}^2\left(R_{k,1} l_j, R_{k,2} m_j\right) \cdot \widetilde{r}_i\left(u_{k,i} R_{k,1} l_j + v_{k,i} R_{k,2} m_j\right). \tag{8}$$

For each subarray $\mathbf{G}_k$ with i, j row–column indices, the $u_{k,i}$ and $v_{k,i}$ baseline coordinates (and their conjugate symmetric pairs) are established by the array element positions during that integration, and the l_j and m_j coordinates are established in the array-centered reference frame. However, the scene image coordinate system cannot be the same as the local l_j, m_j direction cosine coordinates for each $\mathbf{G}_k$, since multiple pointings are used, and a coordinate mapping $R_{k,\{1|2\}}$ must be applied which rotates the image coordinate system to the array centered frame for each integration. $M_{k,j}$ is a coordinate density weighting term determined as the inverse sampling density for the rotated image pixels (from native coordinates) within a uniformly sampled grid of array centered coordinates. Practically, the pattern integration over solid angle, which normalizes the correlation magnitude, is modified to include this term as $\Omega = \sum F^2(l_j, m_j) M_j(l_j, m_j)/(1 - l_j^2 - m_j^2)^{1/2}$.

In principle, a conditioned inversion of composite $\mathbf{G}$ matrix defined (8) could be used to form the image $\mathbf{T}$, where the order of complexity for inversion of an $m \times n$ matrix is $O(m^2 n)$ for m being the greater and n being the lesser of n_v and n_p. This approach to imaging makes sense for a system like SMOS, where a single inversion of $\mathbf{G}$ can be used to form many images. However, in our case, the number of images to be formed is relatively small (as many facets as needed to cover the Antarctic continent). An alternative is to form an image using an iterative cost function optimization approach which requires several forward evaluations of (7), each of complexity $O(n_v n_p)$. This approach has the advantage of leveraging the considerable literature surrounding iterative, nonlinear, regularized methods for solving inverse problems, many of which have been applied in the context of interferometry [60], [61], [62]. Such approaches are capable of mitigating image artifacts, such as Gibbs ripples [63], [64], localizing radio frequency interference (RFI) [65], [66], and attempting image super-resolution [67], [68]. We pose the heterogeneous array imaging inverse problem cost function as follows:

$$\min_T \left(\|\mathbf{GT} - \mathbf{V}\|_2^2 + \lambda R(\mathbf{T}) \right). \tag{9}$$

Equation (9) includes a regularizing term $R(\mathbf{T})$ which weights the cost function toward satisfying a criteria of interest. The contribution of the regularization versus the constraint function is weighted by a value λ. Recent studies have indicated that regularization with respect to image total variation shows good performance in conditioning ill-posed inversions for synthetic aperture imagers with respect to efficiently deconvolving images, preserving edges, and minimizing noise amplification without introducing artifacts [66], [68], [69], [70]. In this case, the form of regularization is

$$R(\mathbf{T}) = \|\nabla \mathbf{T}\|_1 = \sum_{i,j} |\nabla T_{i,j}| \tag{10}$$

which penalizes differences in image gradient magnitudes. To achieve the best results in the final image, a value for the λ parameter must be chosen which obtains a balance between the data constraint and the regularization constraint. We develop an intuition for this trade by demonstrating mosaic imaging of a noise-free scene using the arbitrary sparse array shown in Fig. 4. Synthetic correlations are computed from a reference T_B image of recovery ice stream for nine different observations, each with the array pointing shifted vertically and horizontally with individual overlaps at the beam half-power points. The aggregate field of view pattern is illustrated. From the sparse set of model visibilities, (9) is solved using the split Bregman procedure implementation in the PyLops optimization software package [71] (using an inner loop number of 5 and an outer loop number which achieves convergence, see [72]) with varying values of the weighting term λ, with the results shown in the lower panels of Fig. 7. With no regularization term imposed, the recovered image need only satisfy the sparsely sampled Fourier harmonics and therefore diverges from the true scene considerably. Similarly, over-weighting of the regularization term results in divergence from truth toward satisfying the criteria of minimum variation. We provide further comments on the optimal value for the λ term, the effect of correlation noise, and the impacts of swath overlap spacing in Appendix A.

In summary, we have presented a flexible approach for forming images from mixed pointing and mixed configuration array observations via (8). Equation (9) solves the image stitching problem by comparing the recovered image model directly with the visibility measurements while regularizing variation in spatial structure. The application of total variational regularization has the effect of eliminating any field-of-view boundary artifacts and reducing Gibbs ripples while, as we discuss

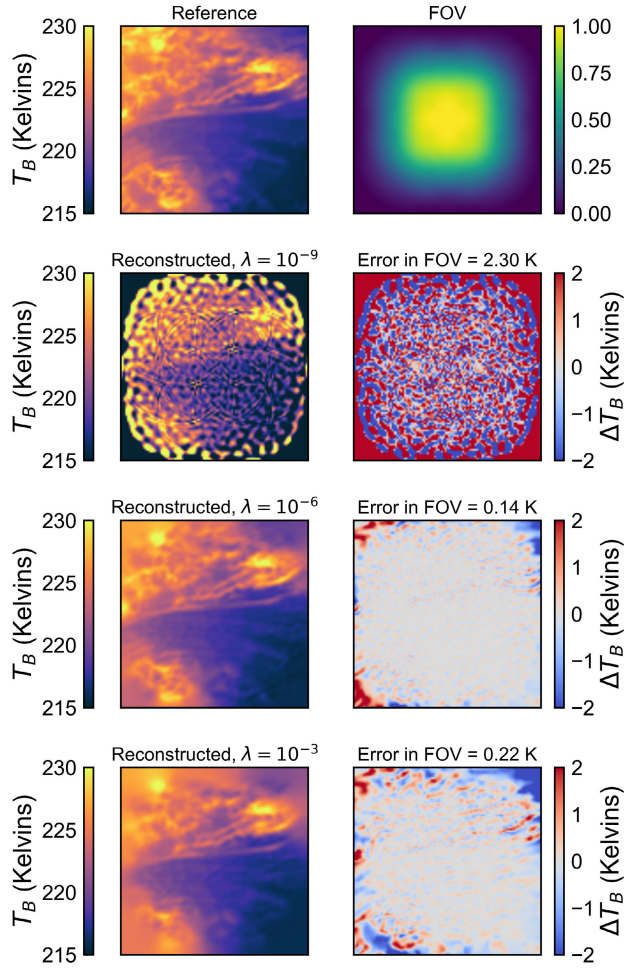

Fig. 7. Demonstration of the Fourier-domain image recovery using noiseless observations with the example sparse array shown in Fig. 4. A reference image from simulations over recovery ice stream is shown, and nine observations of this reference image are made over different regions, with the aggregate array antenna pattern shown in the right of the first row. The image spatial structure is then recovered by solving (9) with different values of the weighting term λ. With minimal regularization ($\lambda = 10^{-9}$ here), the image recovery diverges from the true value due to sparse sampling, whereas with excess regularization ($\lambda = 10^{-3}$ here), the recovered structure is biased toward minimum variation. Errors listed above each comparison chart on the right are computed as the standard deviation of the difference between the reconstructed and reference images.

in Section VI, not compromising entirely the ability of the array measurements to recover small-scale spatial features. However, while this approach is likely more efficient than the inversion of the composite **G** matrix, the computational cost is still nonnegligible, particularly in the case of high-resolution imaging of large facets from many correlation measurements. We defer practical attempts to mitigate this cost to future work, instead providing comments on possible approaches in our concluding remarks.

V. Constellation Design

The results of Section III suggest a spacecraft constellation flying in close proximity and sampling a range of different spatial baselines. We present here a notional constellation design that accomplishes these requirements and uses formation flying simulations to assess the feasibility of such a configuration. We provide in Appendix B some comments on tolerances for position, timing, and data transmission which are relevant for mission design, finding generally that these tolerances can likely be achieved using state-of-the-art technologies.

We consider a three-spacecraft configuration similar to that discussed in [32] set in a circular low-Earth orbit (LEO) of 500-km altitude and 90° inclination with an orbital period equal to 94.6 min. The constellation spacecraft are identical, weighing 500 kg and sized at a 2.5-m radius (assuming a "cannonball" model for simplicity). The choice of a 5-m diameter here is arbitrary, and the minimum size necessary is practically determined by both the size of the array elements and the need to obtain short baseline measurements. The relative motion of the three spacecraft relative to a virtual reference (here the constellation center) is modeled using Clohessy–Wiltshire (CW) dynamics [73], which provide a first-order approximation of the relative motion and are defined in the RTN frame associated with the virtual reference (R: radial direction, Earth to virtual reference, T: transverse/along-track direction, close to orbital velocity vector for circular orbits, and N: normal/cross track: along the orbit angular momentum vector). The CW model is solely used for generating initial conditions for the orbits and the maneuvers, whereas all presented results are generated using high-fidelity propagation of the nonapproximated equations of motion. The included realistic force models are Earth's gravity field (including spherical harmonics up to degree and order 16), Sun and Moon third-body effects, and atmospheric drag using the DTM2000 thermosphere model [74] with variable solar fluxes.

Planar circular orbits (PCOs) are a specific type of periodic relative orbits for which the projection of the motion in the cross-/along-track is a circle [75]. An example of PCO is presented in the RTN frame in Fig. 8(a) with all three spacecraft are spaced 120° apart about a virtual center along the same relative orbit. While a single PCO configuration is relatively stable, it cannot be employed in our context without modification, as the relative configuration of the constellation for each revisit over a given field of view remains fixed.

To maximize the range of baselines generated by the interferometer, we developed a maneuver sequence that uses propulsion to repeatedly cycle through a range of PCOs. The relative configuration cycles between an inner and outer relative orbits using N intermediate orbits as step, as shown in Fig. 8(b). All relative orbits share the same mean motion center (the virtual reference) and orbital semimajor axis. However, their phases are selected to be slightly shifted from each other, as shown in Fig. 8(b). The gray dots denote the locations along the intermediate orbits at time intervals equal to a multiple of the orbital period. Impulsive maneuvers, rather than simple ballistic cycling, are needed to transfer between relative orbits, with two maneuvers occurring per transfer as illustrated in Fig. 8(c). The departure maneuvers (green dots) place the spacecraft on the transfer trajectory, and the insertion maneuvers (red dots) ensure that the spacecraft is inserted into the next relative orbit.

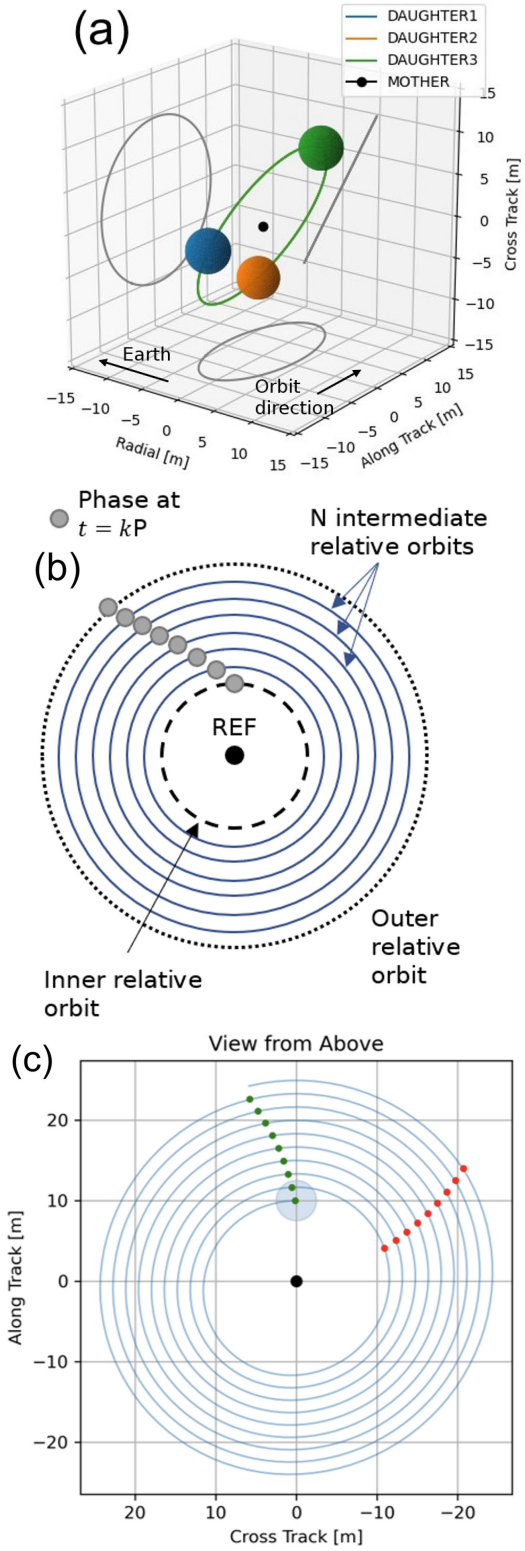

Fig. 8. (a) Illustration of three spacecraft ("daughter") in a PCO configuration in reference to a virtual center ("mother"). (b) Illustration of inner, outer, and intermediate constellation relative orbits. Gray dots denote the locations along the intermediate orbits at time intervals equal to a multiple of the orbital period. (c) Phasing of the transfer (green) and insertion (red) orbit maneuvers employed to transfer between subsequent orbits.

Fig. 9 illustrates the progressive cycling of constellation relative positions and phases between inner and outer orbit shells. For these simulations, the radius of the inner relative orbit is set to 10 m (twice the notional spacecraft diameter), and the radius of the outer relative orbits are chosen as 25 (shown here), 50, and 100 m to correspond to design schemes identified in Section III. Eight intermediate orbits are used between the inner and outer relative orbits, creating a cycle of ten orbits in total.

The collection of passes creates a stroboscopic map (or more informally, a "flower" pattern) of a period equal to the orbital period that outlines the relative location of a spacecraft when it flies over a given latitude (note that the cross-/along-track plane projection does not include the rotation of the Earth). The radii of the inner and outer relative orbits, the number of intermediate orbits, and the difference in phase between consecutive orbits define the number of "petals" and their shapes. In each subfigure in the top row, the color scale represents the pass number, and each dot represents the location of a spacecraft at a time equal to $t = t_0 + kP$, where k is an integer and P is the orbital period. To build the first half of a petal, the constellation moves from the inner relative orbit to the outer relative orbit. The constellation moves through the ten relative orbits at a rate of orbit step per period; therefore, the time-of-flight for the half petal is ten times the orbital period, approximately 16 h. The second half of the petal is created by transferring the constellation from the outer relative orbit back to the inner relative orbit. Due to the design of the intermediate orbits and the selected time-of-flights, each spacecraft does not return to its original phase. The difference in phase along the inner relative orbit creates the base of each petal, as apparent in Fig. 9 (middle). Cycling the constellation between inner and outer relative orbits and back creates a set of three petals; this process is repeated multiple times to create new petals. In Fig. 9, after approximately 70 periods (or five days), the first spacecraft reaches the phase along the inner orbit that the second was in at the initial time. With additional cycle repeats, the space between the inner and outer relative orbits fills in.

Due to the proximity between intermediate relative orbits, the Delta-V required to move between them is very small: each individual maneuver is of the order of mm/s. The total Delta-V cost for the first petal of the first spacecraft (32-h propagation) is about 5 cm/s. This total cost is a function of the distance between consecutive relative orbits and the maximum time-of-flight allowed for each transfer (here 80% of one orbital period, equivalent to 76 min). The total Delta-V costs are 3.94, 10.50, and 23.64 m/s for the 25-, 50-, and 100-m separation constellations, respectively. As the maximum relative orbit radius increases, so does the distance between consecutive orbits, and therefore, so does the total Delta-V cost. Adding intermediate orbits and/or time-of-flights would decrease the total Delta-V cost.

While ignored nonlinear terms in the CW model are typically negligible for small formations such as that considered, atmospheric drag is a source of significant perturbations. Without correction, this additional perturbation is significant enough to cause a potential intraconstellation collision within the first two "petals" of the pattern (or equivalently, the first 2.5 days) as opposed to an un-perturbed case. A tight and

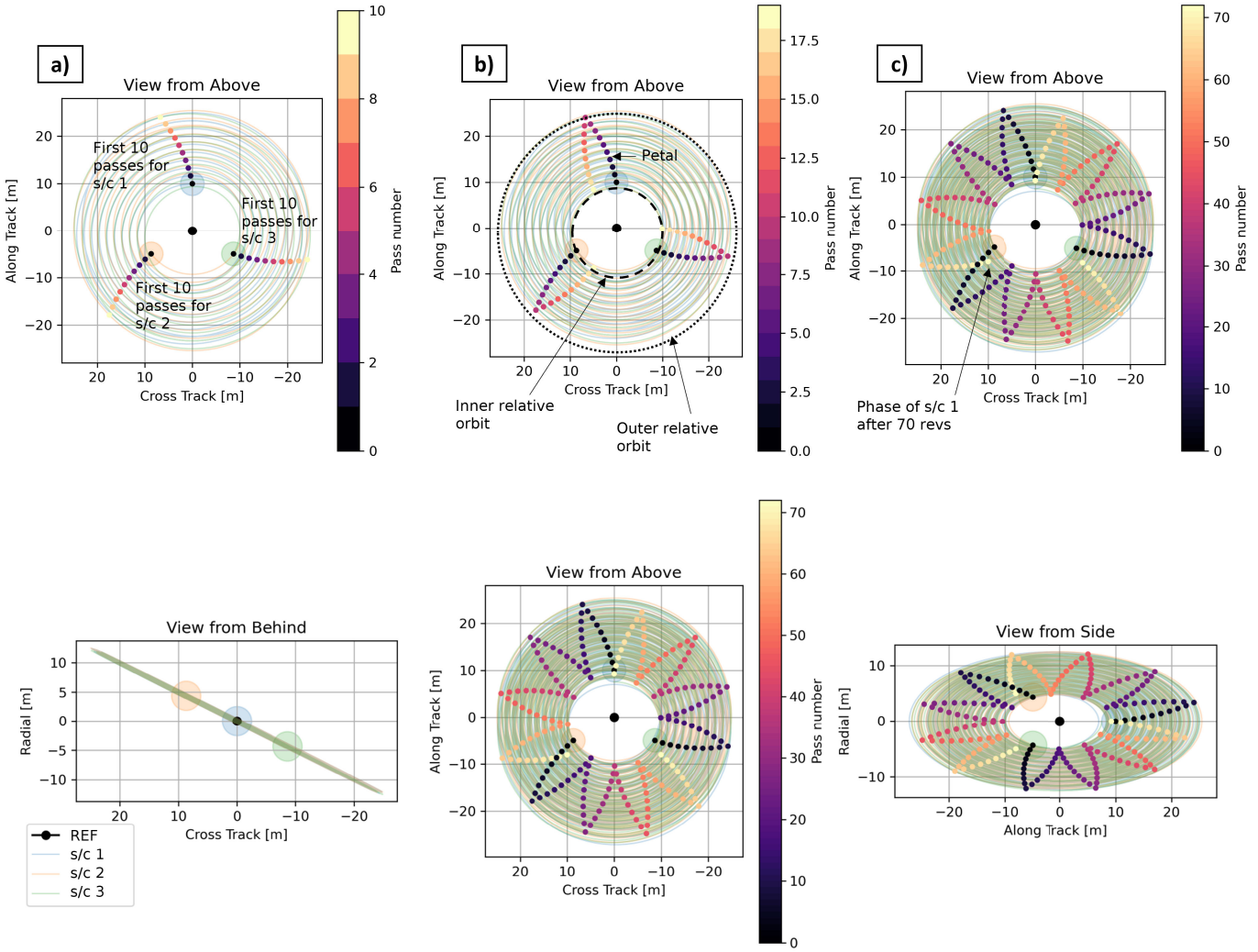

Fig. 9. Assembly of constellation flower pattern, propagated for (a) 16 h, (b) 32 h, and (c) 5 days. The bottom row shows the projection in all planes for the 5-day propagation. Constellation member spacecraft are referred to as s/c 1–3, respectively.

robust control algorithm would therefore be required to maintain the constellation in the flower pattern. The implications of maneuver corrections for a large constellation interferometer are further discussed in [39], finding that such corrections drive the system fuel budget.

VI. Simulated Observations

We now present observing system simulations leveraging the results of previous sections to demonstrate the regional images of Antarctic ice sheet emission which would be recovered from sparse UHF/L-band synthetic aperture radiometry satellite constellation observations. As we show, the results of these simulations are generally consistent with the assessment based on the sensitivity equation in Section III. This simulator operates as follows (see Fig. 10).

1) Array antenna and constellation spacecraft states are used as inputs to SPICE routines which define antenna, array, spacecraft, and Earth system spatiotemporal reference frames and orbits [76]. Orbit tracks are then simulated over a duration of interest.
2) A prescribed geodesic circle is used to mask angle-dependent ice sheet T_B simulation images and select orbit tracks that are relevant for image formation.
3) Once the image region is established, the composite $\mathbf{G}$ matrix (8) is determined from the collection of array field-of-view footprints. We assume in these simulations an ideal antenna field pattern for a uniformly illuminated circular aperture. We also assume an ideal fringe wash function of $\widetilde{r}(ul + vm) = \mathrm{sinc}((B/f)(ul + vm))$. The simulation image coordinate mapping to the array reference frame is inverse-density-weighted in direction cosine space [the M term in (8)].
4) Synthetic correlations are then generated by computing $\mathbf{V}_k = \mathbf{G}_k\mathbf{T}_k$ for each integration and stacking them; this accounts for the emission angle dependence of the scene brightness temperature for each snapshot. For the purpose of recovering a consistent image, a set of approximate incidence angle correction terms is then applied to the composite $\mathbf{G}$ matrix using sheet angular statistics as opposed to the real pixel-level angular dependence.

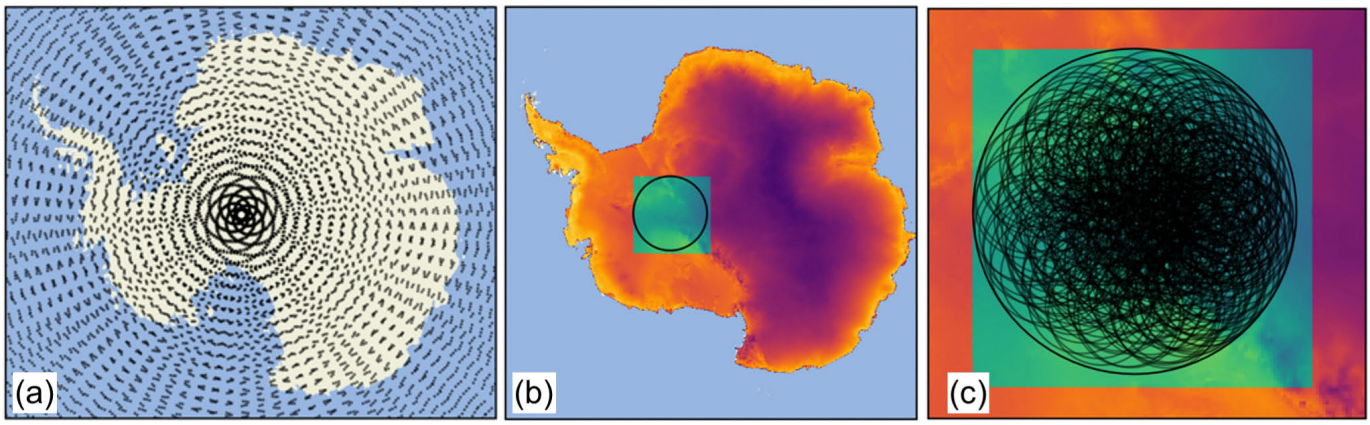

Fig. 10. (a) Illustration of simulation generated orbits, (b) geodesic subsetting of ice sheet brightness temperature simulations, and (c) accumulation of image tracks over this region.

5) Errors are inserted, including thermal noise, errors in array element position/measurement timing, and errors due to heterogeneity in snapshot incidence angle differences.
6) Images are recovered using the iterative approach described in Section IV and compared with the reference quantities to assess the noise performance. The regularization weighting term λ in (9) is determined based on the guidelines in Appendix A.

We conducted observing system simulations for each design scheme discussed in Section III, which are restated as follows.

1) A small aperture (half-wavelength) system consisting of 10–20 antennas that achieves 10-km resolution over the full ice sheet on seasonal-yearly timescales.
2) A medium aperture system (one wavelength) system consisting of 15–25 antennas that achieves 5-km resolution over the full ice sheet on monthly-seasonal timescales.
3) A large aperture system (two wavelengths) consisting of 20–30 antennas which achieve 2-km resolution over the full ice sheet on monthly seasonal timescales.
4) A small/medium aperture system consisting of 3–5 antennas which achieves $<$10 km resolution over the sheet center on seasonal/yearly time scales.

Simulations with schemes 1–3 leverage the constellation designs that were discussed in Section V, ignoring for the moment any differences in mass or shape implied by the chosen array geometries. While the formation flying approach for these schemes is the same, we choose to demonstrate different subarray geometries for each simulation. This is done to illustrate that our multiple-swath sampling approach is applicable to any array layout that satisfies the necessary Fourier sampling density. We provide no comments here on the "optimal" scheme for the subarrays. In addition, we organize each simulation around different aspects of the concept approach which could impact its effectiveness, include the following.

1) The effects of different random and systematic errors on image formation.
2) The efficacy of the image recovery algorithm for recovering small-scale features.
3) The implications of array field of view frequency dependence for image formation.

We caveat our results by acknowledging that our simulations are relatively simple in a few important ways.

1) They present an ideal scene with negligible contributions due to sidelobes, RFI, or backscattered galactic emission.
2) They do not consider antenna, RF signal chain, or correlator nonidealities (see simulations in [77]).
3) In some cases, simulated facets are smaller than the array instantaneous field of view and images are formed from fewer correlations than would be obtained through the relevant design scheme. Since large fields of view, high resolution imaging, and long durations of observing can significantly increase computational costs of evaluating (9), the simulated imaged area and observing time is reduced while accordingly increasing the per-correlation noise as consistent with the quantities in (4).

Nevertheless, we find these simulations sufficiently illustrative of the images that would be obtainable from our proposed concept.

For design scheme 1 (i.e., 1/2 wavelength aperture, 25-m maximum separation, and 10-km spatial resolution), we assess the impacts of different observation error sources on image reconstruction. The chosen array geometry features a large central spacecraft with a 15-element Y-shaped array and two spacecraft with a single element each, and imaging is conducted over a region within the recovery ice stream. This region is smaller than the actual instantaneous field of view associated with 1/2 wavelength elements, and the per-correlation noise is accordingly increased by the ratio of the field of view and imaged region areas. Images are computed from three months' worth of accumulated baselines, and the per-correlation noise is reduced by a factor of 2 to adjust the effective observing time to 1 year. The results of these simulations are shown for 500-MHz T_B in Fig. 11. Fig. 11(c) shows the reference and recovered images following the format of Fig. 7, and Fig. 11(d) shows the relative contribution of different error sources. As the plots proceed in Fig. 11(d), the error residuals from the previous step are subtracted, isolating the effects of each. The top panels in Fig. 11(d) show the errors

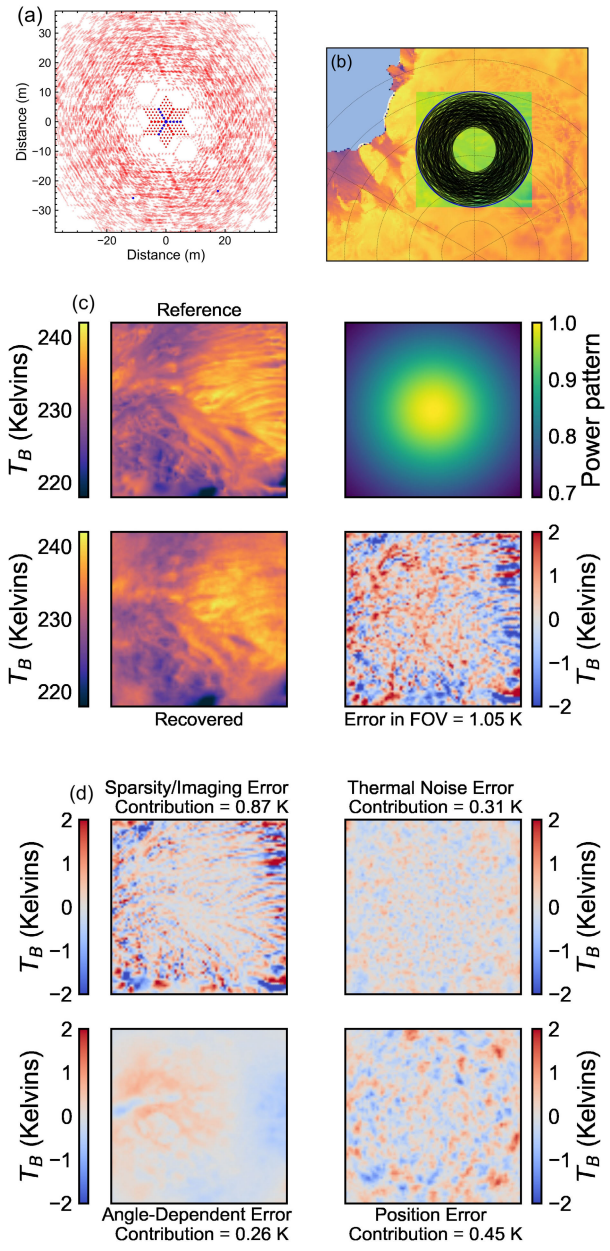

Fig. 11. Scheme 1 simulation experiment. (a) Instantaneous array configuration and accumulated baselines. (b) Imaged scene context (latitude circles drawn every 2.5°). (c) Reference image, aggregate field of view, recovered image, and error in recovery. (d) Contributions to the aggregate error from different elements of the reconstruction, including algorithm thermal noise, angle-dependent emission, and position uncertainty.

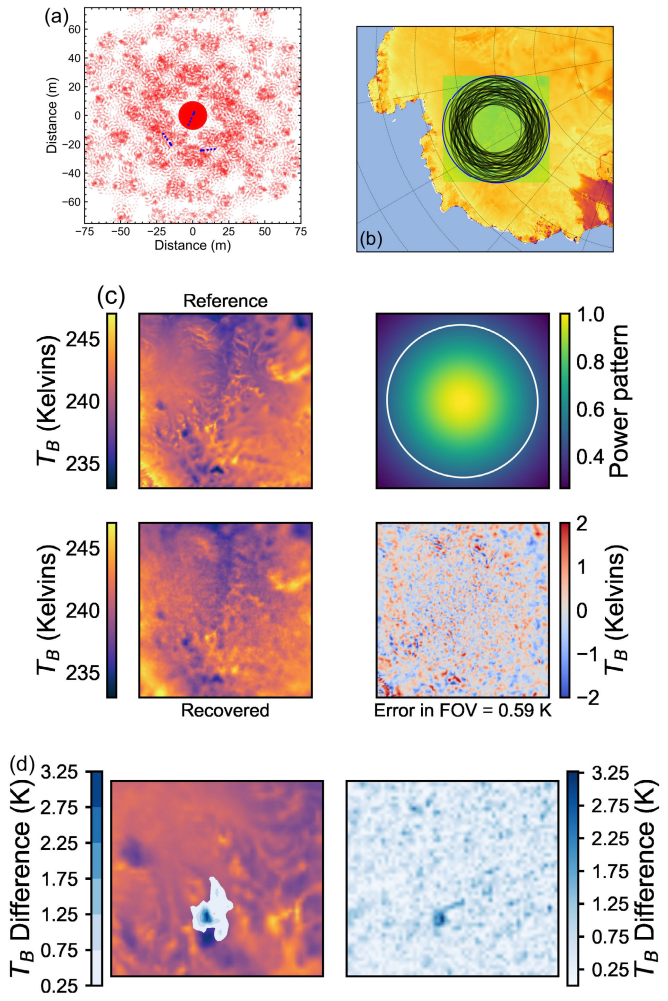

Fig. 12. Scheme 2 simulation experiment. (a) Instantaneous array configuration and accumulated baselines. (b) Imaged scene context (latitude circles drawn every 2.5°). (c) Reference image (without a GHF hotspot), aggregate field of view, recovered image, and error in recovery. (d) (Left) Difference between models and (right) observation simulations of the image scene with and without a 50-km and 200-W/m^2 GHF hotspot (see Appendix C).

resulting from the image recovery approach and thermal noise on the observation. These components are not independent, as the level of thermal noise present in the measured correlation informs the choice of the weight parameter in the imaging regularization (as discussed in Appendix A). The panel on the bottom left of Fig. 11(d) shows the systematic impact of the difference in observation incidence angles between tracks on the recovered image. The results show a systematic spatial bias, but this bias is below 1 K. Finally, the bottom right panel of Fig. 11(d) shows the impact of position errors of order 1 mm on the central location of each spacecraft. The results of these simulations suggest that uncertainty in the knowledge of satellite relative position will have a relatively greater contribution to the overall image uncertainty than knowledge of the pixel-level incidence angle dependence.

For design scheme 2 (i.e., one wavelength aperture, 50-m maximum separation, 10-km spatial resolution), we demonstrate the resolution of a GHF hotspot (50 km and 200 W/m^2) over Thwaites basin with simulated observations. Further simulations of the effects of GHF hotspots with a range of magnitudes and sizes on ice sheet UHF brightness temperatures are provided in Appendix C. Each spacecraft in the constellation includes a seven-element slowly rotating minimum-redundancy array [78]. Images are computed from two months' worth of accumulated baselines, and the per-correlation noise is reduced by a factor of $(3)^{1/2}$ to adjust the effective observing time to six months. The results of these simulations are shown in Fig. 12. To test the capacity for resolving between different scenarios, image synthesis was performed for the reference case and a 50-km and 200-W/m^2 GHF hotspot case, each with different random visibility noise. The left panel of Fig. 12(d) shows the difference in the

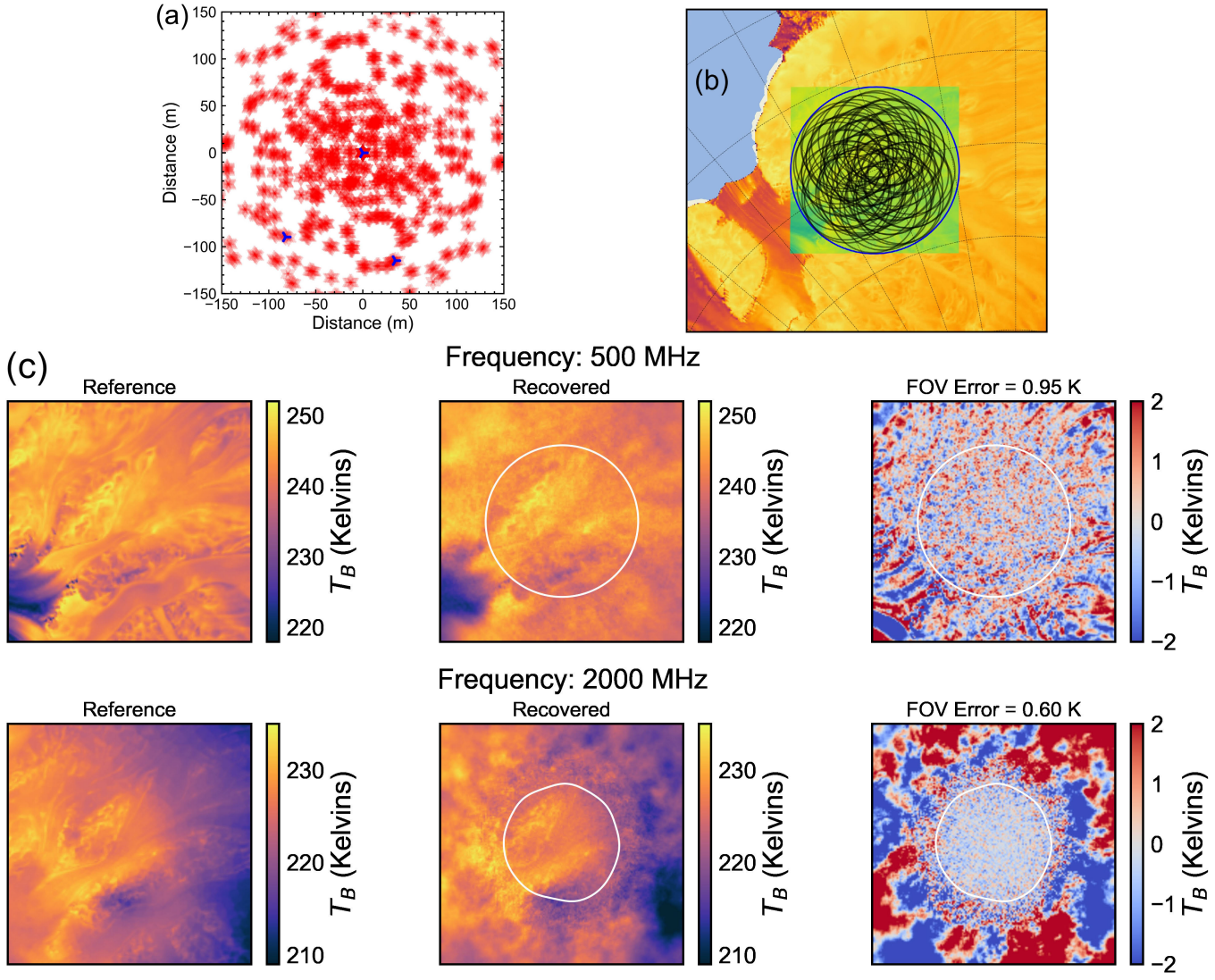

Fig. 13. Scheme 3 simulation experiment. (a) Instantaneous array configuration and accumulated baselines. (b) Imaged scene context (latitude circles drawn every 2.5°). (c) Reference and recovered observations, as well as their differences within the equivalent half-power field of view (shown as a white contour), for 500-MHz and 2-GHz observations.

modeled brightness temperatures imposed over the reference scene, and the right panel shows the difference between simulated noisy observations. This result demonstrates that the total variation regularization strategy adopted for our imaging approach does not reduce the overall capacity to resolve discrete features in a scene.

Simulations for the larger design scheme 3 (i.e., two wavelength aperture, 100-m maximum separation, and 2-km spatial resolution) assess the impact of observing at different wavelengths on the image recovery process. Due to the large aperture, this design scheme is will exhibit significant differences in the instantaneous field of view as a function of frequency. For the chosen array geometry, each spacecraft includes a nine-element Y-shaped array, and simulations were conducted at the edges of the concept frequency range (500 MHz and 2 GHz). Images are computed from two months' worth of accumulated baselines, and the per-correlation noise is reduced by a factor of $(1.5)^{1/2}$ to adjust the effective observing time to three months. The results are shown in Fig. 13, with comparison of the results between the two frequencies in the bottom panels. For the chosen imaging region within the recovery ice stream basin, the aggregate power pattern exhibits different spatial extents, as expected from the frequency dependence of the array field of view. Within the half-power equivalent area of the imaged regions (enclosed in a white contour), however, the image noise is within the expected range. This simulation demonstrates that, while it will be necessary to adjust the number of observations which are used to synthesize an image over a defined region depending on observing frequency, the differences in field of view as a function of wavelength should not degrade the quality of the resulting maps.

Finally, we conduct simulations for design scheme 4. Unlike schemes 1–3, which use the constellation design from Section V, the array geometry here is a set of five independent satellites with a single element co-orbiting in a linear train. The

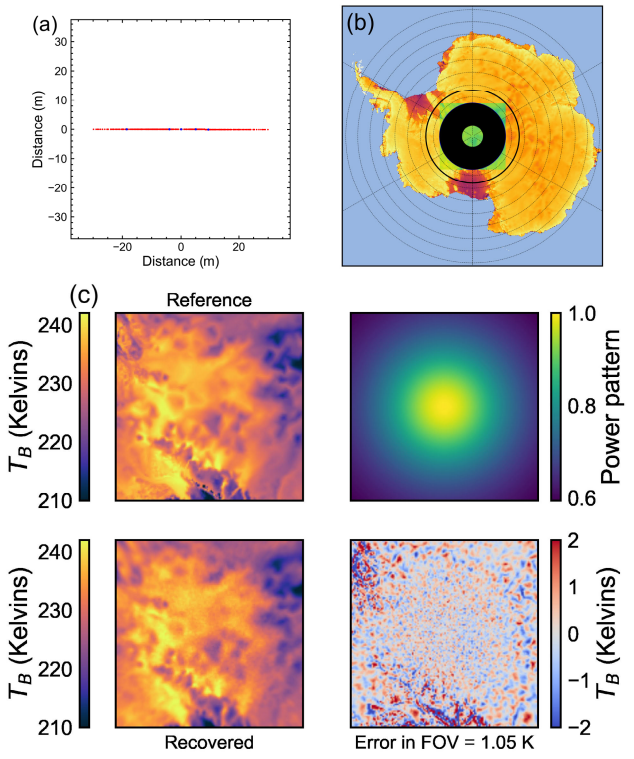

Fig. 14. Scheme 4 simulation experiment. (a) Instantaneous array configuration and accumulated baselines in the array linear reference frame. (b) Imaged scene context (latitude circles drawn every 2.5°) and the broader region observable for this geometry. (c) Reference image, aggregate field of view, recovered image, and error in recovery.

spacings between different satellites are adjusted via periodic oscillation to fill out the necessary range of baselines. As with the scheme 1 simulation, the imaged area is smaller than the actual field of view, and the per-correlation noise is adjusted accordingly. Images are computed from one month's worth of accumulated baselines, and the per-correlation noise is reduced by a factor of $(3)^{1/2}$ to adjust the effective observing time to three months. Fig. 14 shows the results of these simulations directly over the south pole. Since each orbit crosses over the pole from a different direction, baselines are accumulated in two dimensions. For 10-km spatial resolution, a 1-K error is achieved within three months, and higher resolution can be achieved over longer durations at equivalent sensitivity. The full field of view area (defined as the first null width) is shown as the larger circle, illustrating the extent of the ice sheet which could feasibly be resolved for this design scheme. Confirmation of this performance with an on-orbit demonstration would be an important step toward demonstrating a more capable system.

The results of these simulations confirm the general validity of the sensitivity assessment in Section III and argue for the feasibility of our proposed approach. While Appendix C suggests that the regularization of the retrieval should improve the achievable image error over that predicted by (4), the presence of errors due to, e.g., position knowledge and incidence angle dependence offset these gains, bringing the performance back toward that predicted from the sensitivity equation. The further degradation is expected from the incorporation of other instrument nonidealities, but this degradation would not invalidate the fundamental concept feasibility (i.e., they could be offset by relatively minor increases in array complexity).

VII. Conclusion

The results of our investigation suggest that a sparse UHF/L-band synthetic aperture radiometry satellite constellation could be designed to achieve observations of ice sheet temperatures at high spatial resolutions. Such an observing system would represent a significant improvement over the L-band space mission program of record. Our main conclusions are as follows.

1) Thermomechanical and radiative transfer simulations were conducted to develop a high-fidelity model of and to assess the characteristics of ice sheet thermal emission. Seasonal change as predicted by the model and inferred from prior observations suggests that UHF/L-band ice sheet T_B's are stable over yearly timescales within 1 K.
2) An assessment was made of the relationships between array size, observing time, achievable spatial resolution, and sensitivity. Although there is in principle no limit on the achievable spatial resolution given sufficient resources, we determine 1 km as a practical lower bound, requiring on the order of low tens of array elements. Orbits at lower altitudes and array elements with larger ADs are preferred for improving the achievable sensitivity for a given spatial resolution. We determined a highly sparse array design scheme whereby the central 2000-km extent of the ice sheet can be imaged with a linear train of small satellites. This scheme has excellent potential as a technology demonstrator for separated arrays.
3) An imaging approach for mixed pointing/configuration observations was presented that translates the radio astronomy concept of mosaicking into the Earth-sensing context. Our regularized Fourier-domain approach shows excellent performance in the presence of noise and mitigates several undesirable aspects of conventional image inversion procedures.
4) A spacecraft constellation design pattern was developed which can be used to sample a wide range of array baselines gradually over time.
5) Observing system simulations were conducted to explore the effect of different error sources, to demonstrate the resolution of small features, and to assess the impact of instantaneous field of view changes with wavelength on the recovered image.

Several areas warrant further study to mature this concept. An inexhaustive list includes the following.

1) Further ice sheet modeling should be undertaken to illustrate the capacity of wideband L-band observations to resolve between different sheet basal condition and mass loss cases. In addition, further consideration of specific science drivers for very high-spatial resolution observations of ice sheet internal temperatures should be made. We expect this to fall naturally out of the fielding

of any lower resolution UHF/L-band space mission (e.g., CryoRad [17]).

2) Although there is much convenience in our formulation of the image stitching problem, its implementation on a large scale can be computationally expensive. This could be mitigated in several ways.
   a) Developing an approach that permits parallel evaluation of the **GT** product in (9) for subsets of observations within the split Bregman method framework.
   b) Replace the **GT** product with a sequence of gridding and fast Fourier transform operations [79].
   c) Increase the integration time (up to a few seconds total) for each observation by using adjustable delays to compensate for the change in the array phase tracking center during motion [36]. This is valid for field of view overlaps within the half-power width.
   d) Adaptation of visibility coordinate transform methods developed more recently for radio astronomy [59] and Earth remote sensing [80] for multiconfiguration arrays.

   We also encourage further evaluations of the several information-, sparsity-, and scene-based regularization approaches that have been formulated for radio astronomy and Earth sensing applications [58], [62], [81], [82], [83].
3) In the presence of fluctuations in thermospheric density resulting from varying levels of solar flux, the stability of our proposed constellation design significantly decreases. This is potentially the biggest limitation on the concept design. Further efforts should be undertaken in autonomous spacecraft control systems toward correcting for deviations in the state in real time. Furthermore, the constellation simulations presented here should be updated for spacecraft of different shapes/masses.
4) We have omitted the discussion of system calibration. The individual spacecraft could be reoriented for cold sky observations when orbits do not subtend Antarctica, permitting long-duration measurements of system stability, but a more thorough discussion of calibration strategies is likely necessary.
5) At the shortest separations between spacecraft (i.e., closer to 10-km spatial resolution), it is unclear that a separated constellation is preferable to, e.g., an articulating connected array. Possible designs for such systems should be considered.

Appendix A
Considerations for Multiswath Image Reconstruction: Regularization Weighting, Noise, and Swath Overlap

The optimal value for λ in (9) may depend on several factors, including the extent of measurement noise, the geometry of the array, and the inherent complexity of the image. Using the image of recovery ice stream in Fig. 7, we conducted further imaging simulations in which the array size (and thereby number of image pixels), random sampling density (i.e., array layout), and per-correlation noise values were varied, and we subsequently assessed the results of retrievals over a range of different values for λ. Our intent in this search was to determine relationships between these quantities and the optimal value for λ over a representative Antarctic scene. We sought not to determine exact parameterizations, but rather to determine approximate heuristics for application to subsequent simulations.

From these experiments over a single scene, we found the strongest correlation to occur between visibility noise ΔV and optimal regularization weighting λ as $\lambda \propto \Delta V^{1.4\pm0.2}$, exhibiting slight positive covariance with increasing number of image pixels. The quoted exponent range indicates the range of fit values rather than an estimate of errors. Correlations among optimal weighting, image pixel number N_p, and visibility number N_v were not as strong, but results did suggest an inverse correlation for pixel number ($\lambda \propto N_p{}^{-0.8\pm0.6}$) and marginally positive correlation for visibility number ($\lambda \propto N_v{}^{0.3\pm0.4}$). The magnitude for each of these exponents generally decreased with increasing visibility noise. These correlations can be intuitively explained as balancing the total number of counts in the sums for each term in (9); for example, as the total number of pixels increases in an image, the total number of gradient evaluations in (10) will increase, requiring a corresponding decrease in the value of λ to achieve the same relative balance between the measurement constraint and regularization.

We subsequently applied these constraints on the value of λ to the experiment shown in Fig. 7, this time adding noise to the correlations. Fig. 15(a) shows the achieved image error and its value relative to (4). This result highlights both the convergence between our proposed approach and (4) for low noise measurements and the improvements afforded by the total variational regularization for high noise measurements.

Another parameter of interest in our approach is the effect of array instantaneous field-of-view overlap on the resulting stitched image. Using again the case study in Fig. 7, we conduct simulations of the recovered image error for varying levels of correlation noise and scene field of view overlaps. The results, shown in Fig. 15(b), demonstrate that the image noise remains relatively constant until the field-of-view separation increases beyond the half-power width, at which point it begins to increase. This result agrees with the discussion by Cornwell [58] regarding the field-of-view sampling for mosaicking in the radio astronomy context.

Appendix B
Heuristics for Position, Timing, and Data Transmission Tolerances

Thompson et al. [84] present the contribution of different position, timing, and frequency errors to the phase ϕ_{ij} of a correlation measurement of a monochromatic plane wave. This phase error is added to the exponential argument in (1)

$$\phi_{ij} = 2\pi(f - f_{\mathrm{LO}})(\tau_e + \Delta\tau_g) + 2\pi f_{\mathrm{LO}}\Delta\tau_g + 2\pi\Delta f_{\mathrm{LO}}t + \theta_{ji}. \quad (11)$$

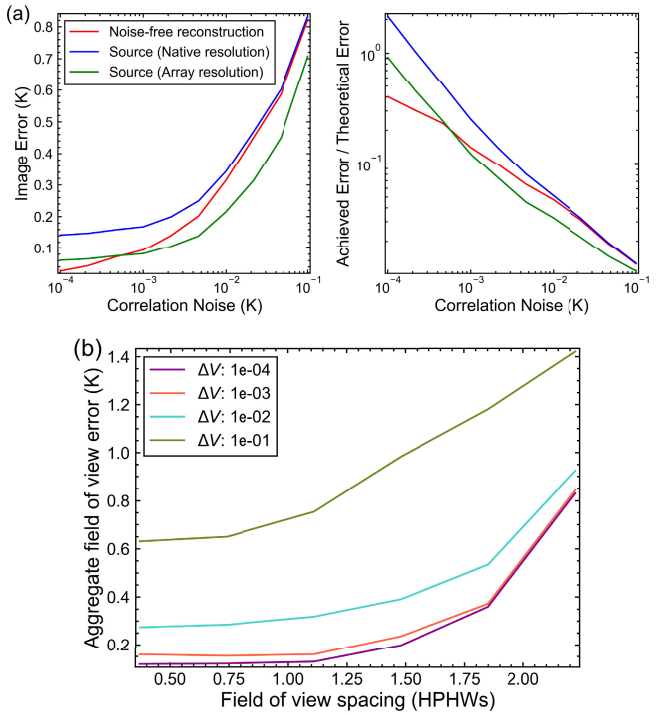

Fig. 15. (a) Image error resulting from solution of (9) for the experiment in Fig. 7 with different levels of per-correlation noise. Different curves show the error in the recovered image relative to the noise-free image reconstruction, the original scene, and the original scene convolved with a Gaussian function fit to the array point spread function. Also shown is the ratio of the achieved noise in the reconstruction with that predicted by (4). (b) Image error from field-of-view overlap tests as a function of field-of-view spacing (in half-power half-widths).

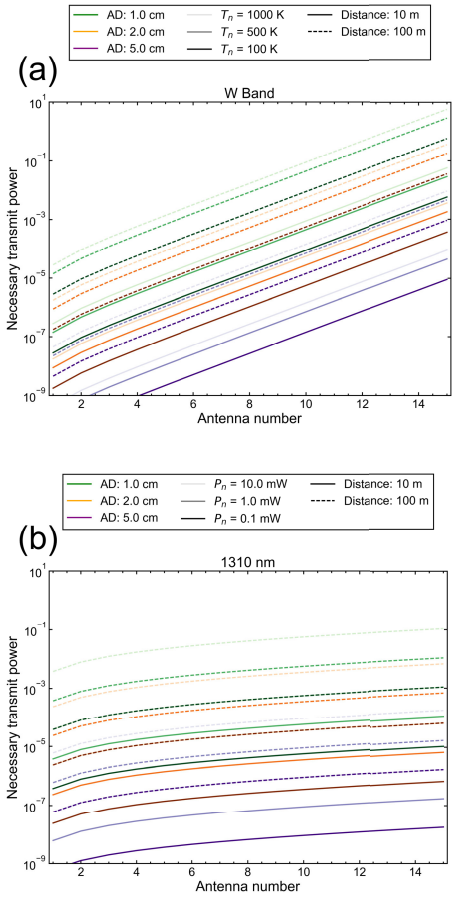

Fig. 16. Transmit power in watts versus number of antennas per satellite for communicating baseband IF measurements to a central correlator using (a) millimeter (W band, 110 GHz) and (b) optical (1310 nm) intersatellite links with different ADs and intersatellite distances.

Here, $2\pi f_{\mathrm{LO}}\ Delta\tau_g = 2\pi\Delta u$ represents the uncertainty in baseline separation (i.e., array element position). For a heuristic acceptable phase error of 1° at 0.5 (2) GHz, this corresponds to required position knowledge on the order of 1.6 (0.4) mm. The factor $2\pi(f - f_{\mathrm{LO}})\tau_e$ represents the sensitivity of the measured phase to clock errors τ_e. In the case of no down-mixing, τ_e should not exceed 2 ps at 2 GHz to limit clock-related phase errors to less than 1°; if signals are mixed to a channel bandwidth of 1.4 MHz, this quantity decreases to 1 ns. Finally, the factor $2\pi\Delta f_{\mathrm{LO}}t + \theta_{ji}$ represents the effect of offsets in LO center frequency offsets Δf_{LO} and phase noise $\theta_{ji} = (\theta_j - \theta_i)$ associated with the array reference oscillator.

Aside from θ_{21}, which is itself a random process, the impacts of position, timing, and frequency offsets in (11) can be calibrated if their temporal variability is relatively slow. For a constellation array, position errors will not be randomly distributed (in which case the aggregate decorrelation becomes order $\langle e^{-j\Delta\phi}\rangle = e^{-\Delta\phi^2/2}$) but will instead manifest as systematic offsets between positions of all array elements on different satellites. These systematic offsets should change relatively slowly compared with offsets arising from the vibrational motion of each spacecraft [85]. Double difference GPS carrier phase measurements have been used to infer relative baselines for the GRACE and TanDEM-X missions with order 1–2-mm accuracy [86], [87]. Intersatellite ranging measurements, however, have demonstrated accuracies on the order of a few micrometers [88], [89]. Since high-rate intersatellite links are required to communicate data to the central correlator, as discussed below, it is not anticipated that position knowledge would be a limiting factor for the array we consider. Time and frequency standards are generated by the same oscillator with Allan deviation σ_y, and from the form of the clock and LO frequency errors, the coherence time can be defined as $t_c = (1 \text{ degree phase})/2\pi f_{\mathrm{LO}}\sigma_y$. Ultrastable oscillators for prior gravimetric missions have obtained Allan deviations on the order of 10^{-13} over timescales of tens of minutes [90], resulting in coherence times on the order of 15 s for measurements at 2 GHz. For the alternative convention of coherence time with respect to $\Delta\phi = 1$ radian, the value is instead nearer to 15 min. Resynchronization of the spacecraft clocks could occur over this timescale via transmission of the reference clock frequency using interspacecraft links.

To form baselines across different spacecraft, raw signal measurements from each element would need to be transferred to the central correlator using wireless links. This could be accomplished via either analog or digital transmission of the Nyquist-sampled signal per spectral channel and antenna via RF/optical modulation. For digital signal transmission, data volumes would accumulate as $N_a b_c f_s N_c N_p$ bits/s, where N_a is the number of antennas, b_c is the number of sample bits, f_s is the sampling frequency, N_c is the number of frequency channels, and N_p is the number of

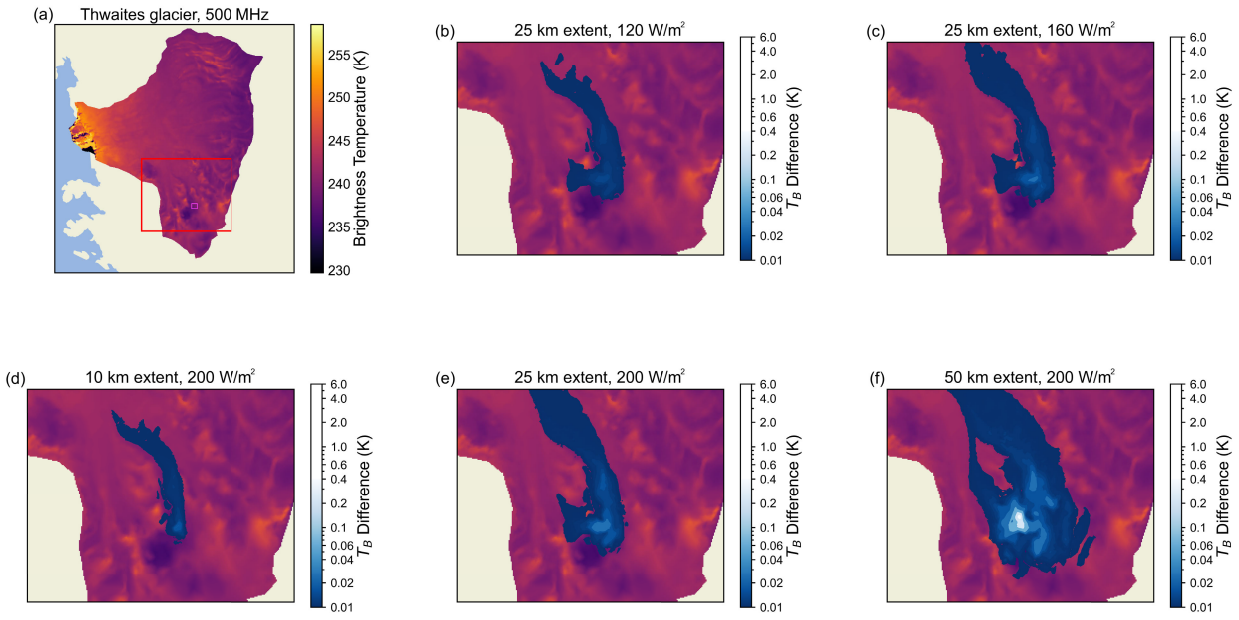

Fig. 17. GHF perturbation simulations over Thwaites basin. (a) High-resolution reference simulation of Thwaites 500-MHz brightness temperature with the perturbation region outlined in pink. (b)–(f) Difference in obtained brightness temperatures [relative to the unperturbed reference simulation in (a)] from simulations with GHF perturbations of various sizes and magnitudes, is shown imposed over the reference image.

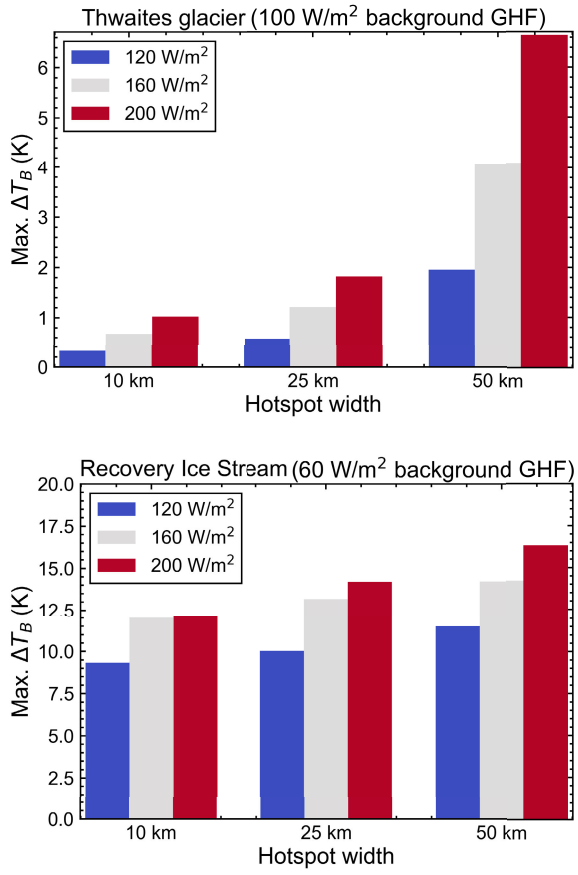

Fig. 18. Maximum difference in 500-MHz brightness temperature between baseline and perturbed simulations for ice sheet emission model test cases including GHF hotspots of arbitrary size and intensity.

observed polarizations. Thus, for single-polarization measurements between 0.5 and 2 GHz with a 1-bit sample fidelity, the data volume is equal to approximately 6-Gbit/s/antenna, all of which must be transferred to and stored on the correlating satellite. Required communications system capabilities in bits/s can be roughly estimated by combining this data rate with the Shannon–Hartley theorem and the Friis transmission equation

$$N_a b_c f_s N_c N_p = B_l \log_2\left(1 + \frac{P_t A_l^2}{P_n d^2 \lambda_l^2}\right). \tag{12}$$

Here, P is the effective transmit and noise powers, A is the effective aperture area, d is the link distance, and the subscript l indicates the corresponding quantity references the communications parameters as opposed to those of the interferometer. Fig. 16 shows different transmission power predicted by (12) as a function of the number of constellation deputy antennas for links at W band (120 GHz and B_l = 6 GHz) and optical (1310 nm and B_l = 50 GHz) frequencies at 10- and 100-m separation. We also consider different receiver noise levels (RF noise temperatures from 100 to 1000 K for RF, and 0.1–10-mW equivalent noise powers for optical) and apertures between 1 and 5 cm, informed by intersatellite communications review articles [91], [92], [93]. While these calculations apply to real-time transmission, data could also be stored locally and then transmitted between satellites later. For collection over Antarctica and retransmission over a half orbit window (permitting time for the downlink of correlated visibilities and calibration procedures), the left side of (12) is reduced by a factor of 1/3 at the cost of $5N_a$ TB onboard storage.

Appendix C
Observability of GHF Hotspots

Regional high-resolution simulations were conducted over Thwaites and the recovery ice stream basins to illustrate

the observability of geothermal hotspots [18]. For distinct locations in each basin, compact regions of elevated GHF are inserted at the base boundary [9], [11], [94]. Specifically, compact regions with GHF values of 120, 160, and 200 W/m^2 are imposed in place of background GHF values of 100 W/m^2 for Thwaites and 60 W/m^2 for recovery. Baseline regional thermal steady-state solves were then repeated for the combination of different values and different sizes of GHF perturbations. MEMLS simulations of the resulting ice temperatures were used to compute the difference in observable T_B at 500 MHz for each feature, with results illustrated for Thwaites in Fig. 17. Of the 0.5–2-GHz frequency range for our concept, the 500-MHz channel was chosen due to its sensitivity to emission from the deepest within the ice sheet. A comparison of the maximum difference in observed T_B's for both Thwaites and recovery simulations shown in Fig. 18 suggests that the effect of GHF hotspots on the observed brightness temperatures depends on the regional environment, specifically background heat flux and the local heterogeneity in topography. Nevertheless, these simulations illustrate that such hotspots are detectable by an observing system achieving image sensitivity on the order of 1 K.

ACKNOWLEDGMENT

The authors gratefully acknowledge NASA's Earth Science Technology Office (ESTO), Washington, D.C. USA, for their support and encouragement of this work.

REFERENCES

[1] T. L. Noble et al., "The sensitivity of the Antarctic ice sheet to a changing climate: Past, present, and future," *Rev. Geophys.*, vol. 58, no. 4, pp. 1–89, Aug. 2020.

[2] E. Rignot, J. Mouginot, and B. Scheuchl, "Ice flow of the Antarctic ice sheet," *Science*, vol. 333, no. 6048, pp. 1427–1430, Sep. 2011.

[3] B. Smith et al., "Pervasive ice sheet mass loss reflects competing ocean and atmosphere processes," *Science*, vol. 368, no. 6496, pp. 1239–1242, Jun. 2020. [Online]. Available: https://www.science.org/doi/10.1126/science.aaz5845

[4] I. Velicogna et al., "Continuity of ice sheet mass loss in Greenland and Antarctica from the GRACE and GRACE follow-on missions," *Geophys. Res. Lett.*, vol. 47, no. 8, pp. 1–8, Apr. 2020, doi: 10.1029/2020GL087291.

[5] A. C. Frémand et al., "Antarctic bedmap data: Findable, accessible, interoperable, and reusable (FAIR) sharing of 60 years of ice bed, surface, and thickness data," *Earth Syst. Sci. Data*, vol. 15, no. 7, pp. 2695–2710, 2023. [Online]. Available: https://essd.copernicus.org/articles/15/2695/2023/

[6] I. Otosaka et al., "Mass balance of the Greenland and Antarctic ice sheets from 1992 to 2020," *Earth Syst. Sci. Data*, vol. 15, no. 4, pp. 1597–1616, Apr. 2023.

[7] G. Macelloni, M. Leduc-Leballeur, F. Montomoli, M. Brogioni, C. Ritz, and G. Picard, "On the retrieval of internal temperature of Antarctica ice sheet by using SMOS observations," *Remote Sens. Environ.*, vol. 233, Nov. 2019, Art. no. 111405, doi: 10.1016/j.rse.2019.111405. [Online]. Available: https://linkinghub.elsevier.com/retrieve/pii/S0034425719304249

[8] A. Burton-Johnson, R. Dziadek, and C. Martin, "Review article: Geothermal heat flow in Antarctica: Current and future directions," *Cryosphere*, vol. 14, no. 11, pp. 3843–3873, Nov. 2020. [Online]. Available: https://tc.copernicus.org/articles/14/3843/2020/

[9] P. Talalay et al., "Geothermal heat flux from measured temperature profiles in deep ice boreholes in Antarctica," *Cryosphere*, vol. 14, no. 11, pp. 4021–4037, Nov. 2020.

[10] Y. M. Martos et al., "Heat flux distribution of Antarctica unveiled," *Geophys. Res. Lett.*, vol. 44, no. 22, pp. 11417–11426, Nov. 2017, doi: 10.1002/2017GL075609.

[11] E. J. Dawson, D. M. Schroeder, W. Chu, E. Mantelli, and H. Seroussi, "Ice mass loss sensitivity to the Antarctic ice sheet basal thermal state," *Nature Commun.*, vol. 13, no. 1, pp. 1–9, Sep. 2022.

[12] I.-W. Park, E. K. Jin, M. Morlighem, and K.-K. Lee, "Impact of boundary conditions on the modeled thermal regime of the Antarctic ice sheet," *Cryosphere*, vol. 18, no. 3, pp. 1139–1155, Mar. 2024.

[13] C. Mätzler, "Microwave dielectric properties of ice," in *Thermal Microwave Radiation: Applications for Remote Sensing*, C. Mätzler, P. W. Rosenkranz, A. Battaglia, and J. P. Wigneron, Eds., London, U.K.: The Institution of Engineering and Technology, 2006.

[14] J. T. Johnson et al., "Microwave radiometry at frequencies from 500 to 1400 MHz: An emerging technology for Earth observations," *IEEE J. Sel. Topics Appl. Earth Observ. Remote Sens.*, vol. 14, pp. 4894–4914, 2021.

[15] K. C. Jezek et al., "500–2000-MHz brightness temperature spectra of the Northwestern Greenland ice sheet," *IEEE Trans. Geosci. Remote Sens.*, vol. 56, no. 3, pp. 1485–1496, Mar. 2018.

[16] C. Yardim et al., "Greenland ice sheet subsurface temperature estimation using ultrawideband microwave radiometry," *IEEE Trans. Geosci. Remote Sens.*, vol. 60, 2022, Art. no. 4300312.

[17] G. Macelloni et al., "Cryorad: A low frequency wideband radiometer mission for the study of the cryosphere," in *Proc. IEEE Int. Geosci. Remote Sens. Symp.*, Jul. 2018, pp. 1998–2000. [Online]. Available: https://ieeexplore.ieee.org/document/8519172/

[18] D. M. Schroeder, D. D. Blankenship, D. A. Young, and E. Quartini, "Evidence for elevated and spatially variable geothermal flux beneath the west Antarctic ice sheet," *Proc. Nat. Acad. Sci. USA*, vol. 111, no. 25, pp. 9070–9072, Jun. 2014, doi: 10.1073/pnas.1405184111.

[19] H. Seroussi, E. R. Ivins, D. A. Wiens, and J. Bondzio, "Influence of a west Antarctic mantle plume on ice sheet basal conditions," *J. Geophys. Res., Solid Earth*, vol. 122, no. 9, pp. 7127–7155, Sep. 2017, doi: 10.1002/2017JB014423.

[20] M. J. Brodzik, B. Billingsley, T. Haran, B. Raup, and M. H. Savoie, "EASE-grid 2.0: Incremental but significant improvements for Earth-gridded data sets," *ISPRS Int. J. Geo-Inf.*, vol. 1, no. 1, pp. 32–45, Mar. 2012.

[21] C. S. Ruf, C. T. Swift, A. B. Tanner, and D. M. Le Vine, "Interferometric synthetic aperture microwave radiometry for the remote sensing of the Earth," *IEEE Trans. Geosci. Remote Sens.*, vol. GRS-26, no. 5, pp. 597–611, Sep. 1988. [Online]. Available: http://ieeexplore.ieee.org/document/7685/

[22] D. M. L. Vine, "The sensitivity of synthetic aperture radiometers for remote sensing applications from space," *Radio Sci.*, vol. 25, no. 4, pp. 441–453, Jul. 1990, doi: 10.1029/RS025i004p00441.

[23] K. D. McMullan et al., "SMOS: The payload," *IEEE Trans. Geosci. Remote Sens.*, vol. 46, no. 3, pp. 594–605, Mar. 2008.

[24] M. Martán-Neira et al., "Microwave interferometric radiometry in remote sensing: An invited historical review," *Radio Sci.*, vol. 49, no. 6, pp. 415–449, Jun. 2014, doi: 10.1002/2013RS005230.

[25] D. M. Le Vine, M. Kao, C. T. Swift, A. Griffis, and A. B. Tanner, "Initial results in the development of a synthetic aperture microwave radiometer," *IEEE Trans. Geosci. Remote Sens.*, vol. 28, no. 4, pp. 614–619, Jul. 1990. [Online]. Available: http://ieeexplore.ieee.org/document/572965/

[26] D. M. Le Vine, T. J. Jackson, and M. Haken, "Initial images of the synthetic aperture radiometer 2D-STAR," *IEEE Trans. Geosci. Remote Sens.*, vol. 45, no. 11, pp. 3623–3632, Nov. 2007.

[27] J. Kainulainen, K. Rautiainen, S. Tauriainen, T. Auer, J. Kettunen, and M. Hallikainen, "First 2-D interferometric radiometer imaging of the Earth from an aircraft," *IEEE Geosci. Remote Sens. Lett.*, vol. 4, no. 2, pp. 241–245, Apr. 2007.

[28] I. Ramos-Perez et al., "PAU-SA: A synthetic aperture interferometric radiometer test bed for potential improvements in future missions," *Sensors*, vol. 12, no. 6, pp. 7738–7777, Jun. 2012. [Online]. Available: http://www.mdpi.com/1424-8220/12/6/7738

[29] A. Tanner, T. Gaier, W. Imbriale, P. Kangaslahti, B. Lambrigtsen, and B. Lim, "A dual-gain design for the geostationary synthetic thinned array radiometer," *IEEE Geosci. Remote Sens. Lett.*, vol. 11, no. 8, pp. 1340–1344, Aug. 2014.

[30] Y. Li, M. Lin, X. Yin, and W. Zhou, "Analysis of the antenna array orientation performance of the interferometric microwave radiometer (IMR) onboard the Chinese ocean salinity satellite," *Sensors*, vol. 20, no. 18, p. 5396, Sep. 2020. [Online]. Available: https://www.mdpi.com/1424-8220/20/18/5396

[31] M. Peichl, H. Suess, M. Suess, and S. Kern, "Microwave imaging of the brightness temperature distribution of extended areas in the near and far field using two-dimensional aperture synthesis with high spatial resolution," *Radio Sci.*, vol. 33, no. 3, pp. 781–801, May 1998.

[32] M. Martín-Neira et al., "TriHex: Combining formation flying, general circular orbits, and alias-free imaging, for high-resolution L-band aperture synthesis," *IEEE Trans. Geosci. Remote Sens.*, vol. 61, 2023, Art. no. 1000317. [Online]. Available: https://ieeexplore.ieee.org/document/10105638/

[33] A. K. S. El Maghraby, A. Grubišić, C. Colombo, and A. Tatnall, "A novel interferometric microwave radiometer concept using satellite formation flight for geostationary atmospheric sounding," *IEEE Trans. Geosci. Remote Sens.*, vol. 56, no. 6, pp. 3487–3498, Jun. 2018.

[34] C. Zhang et al., "Imaging analysis and first results of the geostationary interferometric microwave sounder demonstrator," *IEEE Trans. Geosci. Remote Sens.*, vol. 53, no. 1, pp. 207–218, Jan. 2015.

[35] J. R. Kendra, "Motion-extended array synthesis—Part I: Theory and method," *IEEE Trans. Geosci. Remote Sens.*, vol. 55, no. 4, pp. 2028–2044, Apr. 2017.

[36] A. J. Camps and C. T. Swift, "A two-dimensional Doppler-radiometer for Earth observation," *IEEE Trans. Geosci. Remote Sens.*, vol. 39, no. 7, pp. 1566–1572, Jul. 2001. [Online]. Available: http://ieeexplore.ieee.org/document/934088/

[37] H. Park and Y.-H. Kim, "Microwave motion induced synthetic aperture radiometer using sparse array," *Radio Sci.*, vol. 44, no. 3, pp. 1–12, Jun. 2009.

[38] B. S. Schwarz, A. R. L. Tatnall, and H. G. Lewis, "Coastal salinity measurement using a Doppler radiometer," *Adv. Space Res.*, vol. 50, no. 8, pp. 1138–1149, Oct. 2012, doi: 10.1016/j.asr.2012.01.020.

[39] M. Lützner et al., "Orbit design for a satellite swarm-based motion induced synthetic aperture radiometer (MISAR) in low-Earth orbit for Earth observation applications," *IEEE Trans. Geosci. Remote Sens.*, vol. 60, 2022, Art. no. 1002116.

[40] A. Colliander, M. Mousavi, J. S. Kimball, J. Z. Miller, and M. Burgin, "Spatial and temporal differences in surface and subsurface meltwater distribution over Greenland ice sheet using multi-frequency passive microwave observations," *Remote Sens. Environ.*, vol. 295, Sep. 2023, Art. no. 113705, doi: 10.1016/j.rse.2023.113705.

[41] K. M. Cuffey et al., "Deglacial temperature history of West Antarctica," *Proc. Nat. Acad. Sci. USA*, vol. 113, no. 50, pp. 14249–14254, Dec. 2016.

[42] C. Buizert et al., "Antarctic surface temperature and elevation during the last glacial maximum," *Science*, vol. 372, no. 6546, pp. 1097–1101, Jun. 2021.

[43] M. J. Andrews et al., "The ultrawideband software-defined microwave radiometer: Instrument description and initial campaign results," *IEEE Trans. Geosci. Remote Sens.*, vol. 56, no. 10, pp. 5923–5935, Oct. 2018. [Online]. Available: https://ieeexplore.ieee.org/document/8358015

[44] K. C. Jezek et al., "Radiometric approach for estimating relative changes in intraglacier average temperature," *IEEE Trans. Geosci. Remote Sens.*, vol. 53, no. 1, pp. 134–143, Jan. 2015.

[45] G. Macelloni et al., "Ground-based L-band emission measurements at DOME-C Antarctica: The DOMEX-2 experiment," *IEEE Trans. Geosci. Remote Sens.*, vol. 51, no. 9, pp. 4718–4730, Sep. 2013. [Online]. Available: http://ieeexplore.ieee.org/document/6585775/

[46] M. Leduc-Leballeur et al., "Influence of snow surface properties on L-band brightness temperature at dome C, Antarctica," *Remote Sens. Environ.*, vol. 199, pp. 427–436, Sep. 2017. [Online]. Available: https://linkinghub.elsevier.com/retrieve/pii/S0034425717303504

[47] M. Mousavi, A. Colliander, J. Z. Miller, and J. S. Kimball, "A novel approach to map the intensity of surface melting on the Antarctica ice sheet using SMAP L-band microwave radiometry," *IEEE J. Sel. Topics Appl. Earth Observ. Remote Sens.*, vol. 15, pp. 1724–1743, 2022.

[48] E. Larour, H. Seroussi, M. Morlighem, and E. Rignot, "Continental scale, high order, high spatial resolution, ice sheet modeling using the ice sheet system model (ISSM)," *J. Geophys. Res., Earth Surf.*, vol. 117, no. F1, pp. 1–20, Mar. 2012, Art. no. F01022.

[49] A. S. Gardner, N.-J. Schlegel, and E. Larour, "Glacier energy and mass balance (GEMB): A model of firn processes for cryosphere research," *Geoscientific Model Develop.*, vol. 16, no. 8, pp. 2277–2302, Apr. 2023. [Online]. Available: https://gmd.copernicus.org/articles/16/2277/2023/

[50] C. F. Maule, M. E. Purucker, N. Olsen, and K. Mosegaard, "Heat flux anomalies in Antarctica revealed by satellite magnetic data," *Science*, vol. 309, no. 5733, pp. 464–467, Jul. 2005, doi: 10.1126/science.1106888.

[51] A. Wiesmann and C. Mätzler, "Microwave emission model of layered snowpacks," *Remote Sens. Environ.*, vol. 70, pp. 307–316, Dec. 1999. [Online]. Available: https://linkinghub.elsevier.com/retrieve/pii/S0034425799000462

[52] M. Brogioni et al., "Simulating 0.4–2.5 GHz brightness temperatures of the Ross ice shelf, Antarctica," *IEEE Geosci. Remote Sens. Lett.*, vol. 21, pp. 1–5, 2024. [Online]. Available: https://ieeexplore.ieee.org/document/10443705/

[53] I. Corbella, N. Duffo, M. Vall-llossera, A. Camps, and F. Torres, "The visibility function in interferometric aperture synthesis radiometry," *IEEE Trans. Geosci. Remote Sens.*, vol. 42, no. 8, pp. 1677–1682, Aug. 2004. [Online]. Available: http://ieeexplore.ieee.org/document/1323124/

[54] P. C. Crane and P. J. Napier, "Sensitivity," in *Synthesis Imaging in Radio Astronomy*. San Francisco, CA, USA: Astronomical Society of the Pacific, 1989.

[55] X. Bosch-Lluis, I. Ramos-Pérez, A. Camps, N. Rodriguez-Alvarez, E. Valencia, and H. Park, "Common mathematical framework for real and synthetic aperture by interferometry radiometers," *IEEE Trans. Geosci. Remote Sens.*, vol. 52, no. 1, pp. 38–50, Jan. 2014.

[56] A. B. Tanner and C. T. Swift, "Calibration of a synthetic aperture radiometer," *IEEE Trans. Geosci. Remote Sens.*, vol. 31, no. 1, pp. 257–267, Jan. 1993. [Online]. Available: http://ieeexplore.ieee.org/document/210465/

[57] A. Tanner, T. Gaier, P. Kangaslahti, B. Lambrigtsen, and I. Ramos, "Image synthesis for the GeoSTAR array," in *Proc. 13th Specialist Meeting Microw. Radiometry Remote Sens. Environ. (MicroRad)*, Mar. 2014, pp. 176–180.

[58] T. J. Cornwell, "Radio-interferometric imaging of very large objects," *Astron. Astrophys.*, vol. 202, pp. 316–321, Aug. 1988.

[59] J. Pety and N. Rodríguez-Fernández, "Revisiting the theory of interferometric wide-field synthesis," *Astron. Astrophys.*, vol. 517, pp. 1–21, Jul. 2010.

[60] A. Camps, J. Bará, F. Torres, and I. Corbella, "Extension of the clean technique to the microwave imaging of continuous thermal sources by means of aperture synthesis radiometers," *J. Electromagn. Waves Appl.*, vol. 12, no. 3, pp. 311–313, 1998, doi: 10.1163/156939398X00656.

[61] T. J. Cornwell and K. F. Evans, "A simple maximum entropy deconvolution algorithm," *Astron. Astrophys.*, vol. 143, no. 1, pp. 77–83, Feb. 1985.

[62] B. Picard and E. Anterrieu, "Comparison of regularized inversion methods in synthetic aperture imaging radiometry," *IEEE Trans. Geosci. Remote Sens.*, vol. 43, no. 2, pp. 218–224, Feb. 2005. [Online]. Available: http://ieeexplore.ieee.org/document/1386492/

[63] V. González-Gambau, A. Turiel, E. Olmedo, J. Martínez, I. Corbella, and A. Camps, "Nodal sampling: A new image reconstruction algorithm for SMOS," *IEEE Trans. Geosci. Remote Sens.*, vol. 54, no. 4, pp. 2314–2328, Apr. 2016.

[64] X. Yang, C. Lu, J. Yan, L. Wu, M. Jiang, and L. Li, "Adaptive L^p reconstruction method for synthetic aperture interferometric radiometer," *IEEE J. Sel. Topics Appl. Earth Observ. Remote Sens.*, vol. 15, pp. 3282–3291, 2022. https://ieeexplore.ieee.org/document/9762541/

[65] D. Zhu, J. Li, and G. Li, "RFI source localization in microwave interferometric radiometry: A sparse signal reconstruction perspective," *IEEE Trans. Geosci. Remote Sens.*, vol. 58, no. 6, pp. 4006–4017, Jun. 2020.

[66] J. Preciozzi, A. Almansa, P. Musé, S. Durand, A. Khazaal, and B. Rougé, "A sparsity-based variational approach for the restoration of SMOS images from L1A data," *IEEE Trans. Geosci. Remote Sens.*, vol. 55, no. 5, pp. 2811–2826, May 2017.

[67] M. Piles, A. Camps, M. Vall-llossera, and M. Talone, "Spatial-resolution enhancement of SMOS data: A deconvolution-based approach," *IEEE Trans. Geosci. Remote Sens.*, vol. 47, no. 7, pp. 2182–2192, Jul. 2009. [Online]. Available: http://ieeexplore.ieee.org/document/4806104/

[68] I. Yanovsky, B. H. Lambrigtsen, A. B. Tanner, and L. A. Vese, "Efficient deconvolution and super-resolution methods in microwave imagery," *IEEE J. Sel. Topics Appl. Earth Observ. Remote Sens.*, vol. 8, no. 9, pp. 4273–4283, Sep. 2015. [Online]. Available: https://ieeexplore.ieee.org/document/7109125/

[69] I. Yanovsky and B. Lambrigtsen, "Multispectral super-resolution of tropical cyclone imagery using sparsity-based approaches," *Int. J. Remote Sens.*, vol. 37, no. 11, pp. 2494–2509, Jun. 2016, doi: 10.1080/01431161.2016.1177245.

[70] X. Yang, C. Lu, J. Yan, L. Wu, M. Jiang, and L. Li, "Reweighted total variation regularization based on split Bregman in synthetic aperture imaging radiometry," *IEEE Geosci. Remote Sens. Lett.*, vol. 19, pp. 1–5, 2022. [Online]. Available: https://ieeexplore.ieee.org/document/9663366/

[71] M. Ravasi and I. Vasconcelos, "PyLops—A linear-operator Python library for scalable algebra and optimization," *SoftwareX*, vol. 11, Jan. 2020, Art. no. 100361, doi: 10.1016/j.softx.2019.100361. [Online]. Available: https://linkinghub.elsevier.com/retrieve/pii/S2352711019301086

[72] T. Goldstein and S. Osher, "The split Bregman method for L1-regularized problems," *SIAM J. Imag. Sci.*, vol. 2, no. 2, pp. 323–343, Jan. 2009, doi: 10.1137/080725891.

[73] D. A. Vallado and W. D. McClain, *Fundamentals of Astrodynamics and Applications*, 4th ed., Torrance, CA, USA: Microcosm Press, 2013.

[74] S. Bruinsma, G. Thuillier, and F. Barlier, "The DTM-2000 empirical thermosphere model with new data assimilation and constraints at lower boundary: Accuracy and properties," *J. Atmos. Solar-Terrestrial Phys.*, vol. 65, no. 9, pp. 1053–1070, Jun. 2003.

[75] K. T. Alfriend, H. Schaub, and D.-W. Gim, "Gravitational perturbations, nonlinearity, and circular orbit assumption effects on formation flying control strategies," in *Proc. AAS Guid. Control Conf.* Breckenridge, CO, USA: AAS, 2000, pp. 1–20.

[76] C. Acton, N. Bachman, B. Semenov, and E. Wright, "A look towards the future in the handling of space science mission geometry," *Planet. Space Sci.*, vol. 150, pp. 9–12, Jan. 2018, doi: 10.1016/j.pss.2017.02.013.

[77] A. Camps et al., "Microwave imaging radiometers by aperture synthesis performance simulator (Part 2): Instrument modeling, calibration, and image reconstruction algorithms," *J. Imag.*, vol. 2, no. 2, p. 18, May 2016.

[78] M. Ishiguro, "Minimum redundancy linear arrays for a large number of antennas," *Radio Sci.*, vol. 15, no. 6, pp. 1163–1170, Nov. 1980.

[79] U. Rau, S. Bhatnagar, M. A. Voronkov, and T. J. Cornwell, "Advances in calibration and imaging techniques in radio interferometry," *Proc. IEEE*, vol. 97, no. 8, pp. 1472–1481, Aug. 2009. [Online]. Available: http://ieeexplore.ieee.org/document/5109712/

[80] M. Dunitz et al., "Multisnapshot imaging for LIIFE: Along-the-track inversion of the Van Cittert-Zernike theorem for unfolding and denoising," in *Proc. IEEE Conf. Antenna Meas. Appl. (CAMA)*, Nov. 2023, pp. 457–462. [Online]. Available: https://ieeexplore.ieee.org/document/10352689/

[81] Y. Wiaux, L. Jacques, G. Puy, A. M. M. Scaife, and P. Vandergheynst, "Compressed sensing imaging techniques for radio interferometry," *Monthly Notices Roy. Astronomical Soc.*, vol. 395, no. 3, pp. 1733–1742, May 2009, doi: 10.1111/j.1365-2966.2009.14665.x.

[82] L. Medeiros, T. R. Lauer, D. Psaltis, and F. Özel, "Principal component analysis as a tool for characterizing black hole images and variability," *Astrophysical J.*, vol. 864, no. 1, p. 7, Sep. 2018, doi: 10.3847/1538-4357/aad37a.

[83] R. Faucheron, E. Anterrieu, L. Yu, A. Khazaal, and N. J. Rodríguez-Fernández, "Deep-learning-based approach in imaging radiometry by aperture synthesis: An alias-free method," *IEEE J. Sel. Topics Appl. Earth Observ. Remote Sens.*, vol. 17, pp. 6693–6711, 2024.

[84] A. R. Thompson, J. M. Moran, and G. W. Swenson, *Interferometry and Synthesis in Radio Astronomy* (Astronomy and Astrophysics Library). Berlin, Germany: Springer, 2017, doi: 10.1007/978-3-319-44431-4.

[85] A. Camps, J. Bará, F. Torres, I. Corbella, and J. Romeu, "Impact of antenna errors on the radiometric accuracy of large aperture synthesis radiometers," *Radio Sci.*, vol. 32, no. 2, pp. 657–668, Mar. 1997, doi: 10.1029/96RS03198.

[86] R. Kroes, O. Montenbruck, W. Bertiger, and P. Visser, "Precise GRACE baseline determination using GPS," *GPS Solutions*, vol. 9, no. 1, pp. 21–31, Apr. 2005.

[87] A. Jäggi et al., "Inter-agency comparison of TanDEM-X baseline solutions," *Adv. Space Res.*, vol. 50, no. 2, pp. 260–271, Jul. 2012.

[88] M. Murböck, P. Abrykosov, C. Dahle, M. Hauk, R. Pail, and F. Flechtner, "In-orbit performance of the GRACE accelerometers and microwave ranging instrument," *Remote Sens.*, vol. 15, no. 3, p. 563, Jan. 2023.

[89] K. Abich et al., "In-orbit performance of the GRACE follow-on laser ranging interferometer," *Phys. Rev. Lett.*, vol. 123, no. 3, p. 31101, Jul. 2019, doi: 10.1103/physrevlett.123.031101.

[90] D. G. Enzer, R. T. Wang, and W. M. Klipstein, "GRAIL—A microwave ranging instrument to map out the lunar gravity field," in *Proc. IEEE Int. Freq. Control Symp.*, Jun. 2010, pp. 572–577.

[91] H. Lim, J. Park, M. Choi, C. Choi, J. Choi, and J. Kim, "Performance analysis of DPSK optical communication for LEO-to-ground relay link via a GEO satellite," *J. Astron. Space Sci.*, vol. 37, no. 1, pp. 11–18, Mar. 2020. [Online]. Available: http://www.janss.kr/archive/view

[92] G. Morthier, G. Roelkens, and R. Baets, "Optical versus RF free-space signal transmission: A comparison of optical and RF receivers based on noise equivalent power and signal-to-noise ratio," *IEEE J. Sel. Topics Quantum Electron.*, vol. 28, no. 2, pp. 1–8, Mar. 2022.

[93] A. J. Alqaraghuli, J. V. Siles, and J. M. Jornet, "The road to high data rates in space: Terahertz versus optical wireless communication," *IEEE Aerosp. Electron. Syst. Mag.*, vol. 38, no. 6, pp. 4–13, Jun. 2023.

[94] M. Lösing, J. Ebbing, and W. Szwillus, "Geothermal heat flux in Antarctica: Assessing models and observations by Bayesian inversion," *Frontiers Earth Sci.*, vol. 8, pp. 1–13, Apr. 2020, doi: 10.3389/feart.2020.00105.